NTNU – Trondheim
Norwegian University of
Science and Technology

The Effect of Vanadium on AlFeSi - Intermetallic Phases in a Hypoeutectic Al-Si Foundry Alloy

Elin Schonhovd Dæhlen

Chemical Engineering and Biotechnology
Submission date: June 2013
Supervisor: Lars Arnberg, IMTE
Co-supervisor: Thomas Hartmut Ludwig, IMT

Norwegian University of Science and Technology
Department of Materials Science and Engineering

Declaration

I hereby declare that the work presented in this document has been performed independently and in accordance with the rules and regulations of the Norwegian University of Science and Technology (NTNU).

Trondheim, 14 June 2013

Elin Schonhovd Dæhlen

Acknowledments

Hydro Aluminium AS is acknowledged for funding the Ph.D. work for Thomas Ludwig and thereby also indirectly this master thesis, and for supplying materials and analysing alloys. Vigeland Metall AS and Wacker-Chemie are thanked for supplying HP-aluminium and SG-silicon for the experiments.

A great thanks is rewarded co-supervisor Thomas Ludwig for answering questions of any size even during his stay abroad. The patient people at the NTNU EM-lab, especially Yingda Yu, must receive a thanks for never turning away questions when I ran down the door to the lab. The metallurgy lab personnel, Erlend Nordstrand and Torill Krogstad, is also mentioned for dealing with my minor metallographic related crises.

In connection with my futile attempt at doing TEM, Ph.D. students Sindre Bunkholdt and Sigurd Wenner is thanked for explaining and guiding in the procedure for preparing TEM samples. Sintef researcher Yanjun Li is thanked for helping out with operation of the TEM.

Finally, main supervisor Lars Arnberg is thanked for allowing a chemist into the world of aluminium and casting by coming up with the idea for this project when I came knocking on his door. I also wish to thank Ole Jørgen Østensen who is directly responsible for leading me into casting in the first place by enthusiasticly encouraging me to take Lars' casting course at NTNU. Without his convincing arguments no one knows where I would have ended.

Abstract

The effect of Vanadium on the Fe-rich α and β intermetallic particles in a high purity Al-7wt% foundry alloy was investigated. Needle- and Chinese script-like Fe-rich intermetallic particles were successfully identified as monoclinic β-$Al_{4.5}FeSi$ and hexagonal α-Al_8Fe_2Si, respectively, by EBSD and atomic Fe/Si-ratios measured by EDS. V was found to accumulate in the α-phase and the content increased with increasing V-content in the alloy.

For alloys containing 0.3wt% Fe cast at a low cooling rate (0.3 K/s) the average area fraction of α relative $\alpha + \beta$ increased with increasing V-content in the alloy and the average total area of intermetallic particles decreased. For alloys containing 0.3wt% Fe cast at a high cooling rate (0.9 K/s) the average area fraction of α relative $\alpha + \beta$ was very high and decreased with increasing V-content in the alloy and the average total area of intermetallic particles increased from 0 to 600ppm V and decreased from 600ppm to 0.2wt% V. Addition of a TiB_2 grain refiner caused more and larger β-needles in the 0.2wt% V alloy. The changes were explained by stabilization of the α-phase in the Al-Fe-Si phase diagram by V-additions, similar to the effect of Mn-additions.

Sammendrag

Effekten av Vanadium på Fe-holdige α og β intermetalliske partikler i en høy renhets Al-7wt% Si legering ble undersøkt. Nåle- og Kinesisk skrift- lignende Fe-holdige intermetalliske partikler ble identifisert som henholdsvis monoklin β-$Al_{4.5}FeSi$ og heksagonal α-Al_8Fe_2Si på grunnlag av EBSD og det atomiske Fe/Si-forholdet målt med EDS. V viste seg å akkumulere i α-fasen og innholdet økte med økt V-innhold i legeringen.

For legeringer med 0.3wt% Fe støpt ved lav avkjølingshastighet (0.3 K/s) økte den gjennomsnittlige arealfraksjonen av α relativt til $\alpha + \beta$ med økende V-innhold i legeringen, og det gjennomsnittlige totale arealet av intermetalliske partikler avtok. For legeringer med 0.3wt% Fe støpt ved høy avkjølingshastighet (0.9 K/s) var den gjennomsnittlige arealfraksjonen av α relativt til $\alpha + \beta$ svært høy og avtagende med V-innholdet i legeringen, og det gjennomsnittlige totale arealet av intermetalliske partikler økte fra 0 til 600ppm V og avtok fra 600ppm V til 0.2wt% V. Tilsats av en TiB_2 kornforfiner til legeringen med 0.2wt% V medførte fler og større β-nåler. Forandringene ble forklart som stabilisering av α i Al-Fe-Si fasediagrammet som følge av V, lignende forandringen som skjer ved Mn tilsatser.

Table of Contents

Abbreviations

Abbreviation	Definition
CI	Confidence Index
EBSD	Electron BackScatter Diffraction
EDS	Energy Dispersive Spectrometer
GR	Grain Refiner
OES	Optical Emission Spectroscopy
OIM	Orientation Imaging Microscopy (EBSD offline analysis software)
OP-AN	Neutral alumina suspension for final sample polishing
OP-S	Chemical etching solution for final sample polishing
P/B	Peak to Background
ppm	Parts per million
SE	Secondary electrons
SEM	Scanning Electron Microscope
XRF	X-Ray Fluorescence
ZAF	Atomic number (Z), absorption (A) and Fluorescence (F)

Symbols

Symbol	Definition
a	A unit cell side length in crystal structure
b	A unit cell side length in crystal structure
β-angle	Angle between unit cell sides a and c in a crystal structure
C_l	Concentration in liquid
C_0	Initial concentration in melt
ΔT	Undercooling at solidification
f_s	Fraction solidified
k	Distribution coefficient
Fe_{crit}	Critical Fe concentration above which binary eutectic β forms
λ	Eutectic lamellar spacing
V	Growth rate
V	Vanadium

Chapter 1

Introduction

Aluminium alloys have a wide range of applications, due to their combination of low weight and high strength. The different alloys are classified into series based on the alloying elements and their typical range. One such series, the common 3xx.x foundry alloys is based on the Al-Si system with Si contents typically in the range of 5 to 22wt% [1]. These alloys have very good castability, high strength and good wear resistance, making them suitable for several automotive applications such as engine blocks and rims [2, 3]. Closely related to the 3xx.x casting alloys are the 6xxx wrought alloys series. These alloys are based on the Al-Mg-Si system with Si content commercially around 0.2 to 1.7wt% and Mg levels 0.35 to 1.5wt% Mg [1]. They are used in the production of structural parts by forging, extruding or rolling [1]. The performance of both alloy types relies on the structure of the Al-Si eutectic as well as the presence and distribution of intermetallic phases forming in these complex multicomponent systems [2].

Iron is a common impurity element in Al alloys and is often regarded as detrimental due porosity formation and formation of Fe-containing intermetallic particles which can function as crack initiation points [4, 5]. It is, however, used as an alloying element in certain wrought alloys as it improves e.g. the properties of the final product due to the formation of the α-phase [4], or prevents die soldering during high-pressure die-casting of Al-Si foundry alloys [6]. Fe enters the primary aluminium products through both the Bayer Process where iron oxides is present in the ore and the Hall-Hèroult process where iron is present in the coke used for anodes. Iron may also stem from alloying elements and recycled scrap. There is no commercial method to efficiently reduce Fe-levels and therefore Fe is inevitable in final aluminium alloy components [4].

The resulting ternary Al-Si-Fe system is complex with many different binary and ternary intermetallic phases forming and interacting with each other. The ternary phases include the seaweed shaped (Chinese script-like in 2D) α-Al_8Fe_2Si and the platelet shaped (needles

in 2D) β-Al_5FeSi phases. The β-phase is considered to be detrimental to the mechanical properties of aluminium alloys as it forms hard and brittle needles [5, 7]. This is a problem as β normally forms at the cooling rates obtained during casting in sand and permanent moulds [8].

Factors influencing the precipitation of the β-phase have been investigated thoroughly. It was found that the formation and size of the intermetallic platelets are affected by cooling rate in both alloy systems [9, 10]. The Fe-and Si-content will also influence the amount of β formed [9, 11, 12]. Investigations of the nucleation mechanism of the Al-Si eutectic claim that β-phase particles might serve as nucleation sites for the eutectic Si [13]. On the other hand, pre-existing particles such as AlP and TiB_2 which are distributed homogeneously in the melt prior to any primary Al or Si solidification, may promote the formation of the Fe-rich intermetallic phases [14, 15].

Initial investigations of Fe-rich intermetallic particles yielded many different stoichiometric compositions and revealed disagreements on crystal structures, a summary of which can be found e.g. in the work by Obinata [16]. The result is several phase misinterpretations and a wide variety of nomenclatures for the same particles. E.g. the α- and β-phase can be found as τ_5 and τ_6, which again can be found as K_5 and K_6 as proposed by Takeda et al. [17].

The α-phase is now accepted to be Al_8Fe_2Si with a hexagonal structure. With the presence of Mn the α-particles are stabilized by Mn exchanging for some of the Fe atoms. This causes the α-area in the phase diagram to expand on expense of the β-phase [18, 19, 20]. This causes a transition into a body centred cubic structure which has been reported with varying stoichiometric compositions, e.g. $Al_{15}(Fe,Mn)_3Si_2$ [4] and $Al_{19}(Fe,Mn)_5Si_2$ [21]. The β-phase has been found to have a solubility range for Mn as well but the concentrations reported are lower compared to the α-phase [22, 23]. Following this the existence of the Al_5(Fe,Mn)Si-phase has been suggested [22]. However, structural analysis of the Mn containing β-phases by EBSD indicate a tetragonal Al_3(Fe,Mn)Si_2 [24], a needle shaped particle more commonly known as δ-phase [21].

The transition from a hexagonal to a cubic α-phase was shown by Munson [25] to be promoted by trace additions of impurity elements e.g. V, Cr, Mo, W and Cu as well as Mn. Due to the good high temperature properties of Al-Fe-V-Si alloys because of favourable dispersoids forming upon rapid solidification, these alloys have been investigated extensively. Skinner et al. [26] reported that V stabilizes the α-dispersoids by precipitation of the cubic $Al_{12}(Fe,V)_3Si$ phase in a rapidly solidified, low Si (1 to 2.28wt%) melt spun alloy. Rodriguez and Skinner [27] extracted α-dispersoids from the same alloy and identified two cubic phases with different stoichiometries, $Al_{12.86}(Fe,V)_{3.0}Si_{2.1}$ and $Al_{13.37}(Fe,V)_{3.0}Si_{1.11}$. Further structure analysis showed that V atoms stabilizes the crystal structure by partly or completely replacing Fe atoms in the α-phase. [28].

The effect of V on Fe-rich particles has not been addressed specifically yet. However, accumulation of V in needle-like intermetallic particles with a stoichiometry resembling the atomic ratios of the β-phase were reported in a foundry alloy containing 0.9wt% Si, 8.3wt% Fe and 0.8wt% V [29]. Still, most of the work concerning V and α- and/or β-AlFeSi has been done in wrought alloy systems. Literature focusing solely on foundry alloys is rather scarce.

More recently attention has been paid to the accumulation of Ni and V in the primary aluminium due to the increasing Ni and V levels in the coke used in the anodes [30]. The investigations focused on V distribution and grain structure [31], V removal kinetics [32] and corrosion and mechanical effects [33]. The aim of the present investigation is to study the effect of vanadium additions on the phase selection of Fe-rich intermetallics in a high purity Al-7wt% foundry alloy.

Chapter 2

Theory

2.1 Solidification in the Al-Si-Fe system

2.1.1 Phase diagrams

The binary phase diagrams for Al-Si, Al-Fe and Fe-Si are shown in Appendix A. Based on these diagrams there are 9 binary intermetallic phases that can form in addition to the Al-Si eutectic and the metal phases Al and Fe.

Several ternary intermetallic phases may form in the ternary system and the full ternary diagram is rather complex. Therefore, the diagram for the Al-rich corner which is relevant for the investigation at hand, is given in Figure 2.1. In this figure the phases α and β are called τ_5 and τ_6, respectively. A liquidus projection of the ternary phase diagram is given in Figure 2.2 with solidification paths for a 7wt% Si and 0.1wt%Fe alloy and a 7wt% Si and 0.3wt% Fe alloy.

Since the alloy investigated in the present report is a high purity Al-7wt% Si alloy with maximum 0.3wt% Fe added, the alloy composition will be very close to the Al-Si line (right side of the diagram) in Figure 2.1. Several reactions are indicated in the ternary diagrams and one of the most important for the current investigation is the ternary eutectic reaction E_1, Al + Si + β.

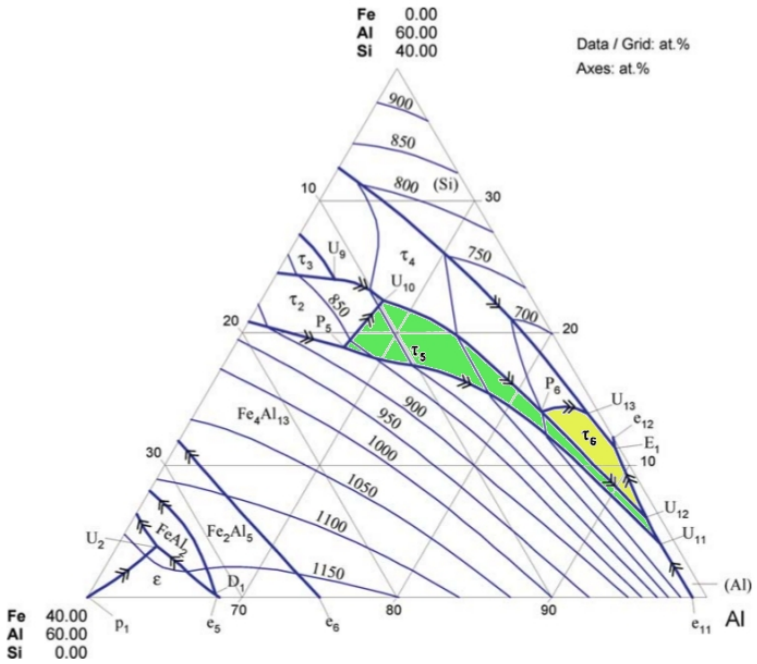

Figure 2.1: Ternary phase diagram for Al-Fe-Si in the Al-rich corner as given in [34] based on the work of Takeda et al. [17]. The τ_5-phase equals the α-phase and the region is marked as green. The yellow region is the τ_6-phase which equals the β-phase.

During solidification the iron and silicon will be rejected into the residual liquid due to the low solubility in the solid Al-phase [7]. This can also be seen from the binary phase diagram for Al-Fe in Figure A.2 in Appendix A. If the solid solubility is assumed to be zero and the equilibrium condition is applied, the Scheil equation, shown in Equation 2.1 [7], may be applied.

$$C_l = C_0(1 - f_s)^{k-1} \tag{2.1}$$

where C_l is the average concentration of the element in the remaining liquid, C_0 is the initial concentration of the element in the alloy, f_s is the fraction solidified and k is the distribution coefficient (based on the phase diagram).

This equation may be plotted in the phase diagram for different initial concentrations of Fe to give an estimation of the solidification path. An example of this, given by Taylor [4] for an alloy containing 0.8wt% Fe, is shown in Figure 2.3. It suggests that under the present assumptions, Al dendrites would form before the binary eutectic Al + β, and then finally the main eutectic Al + Si + β (B) is reached. No α is therefore predicted. For alloys containing less Fe a similar path would result, also without any α forming.

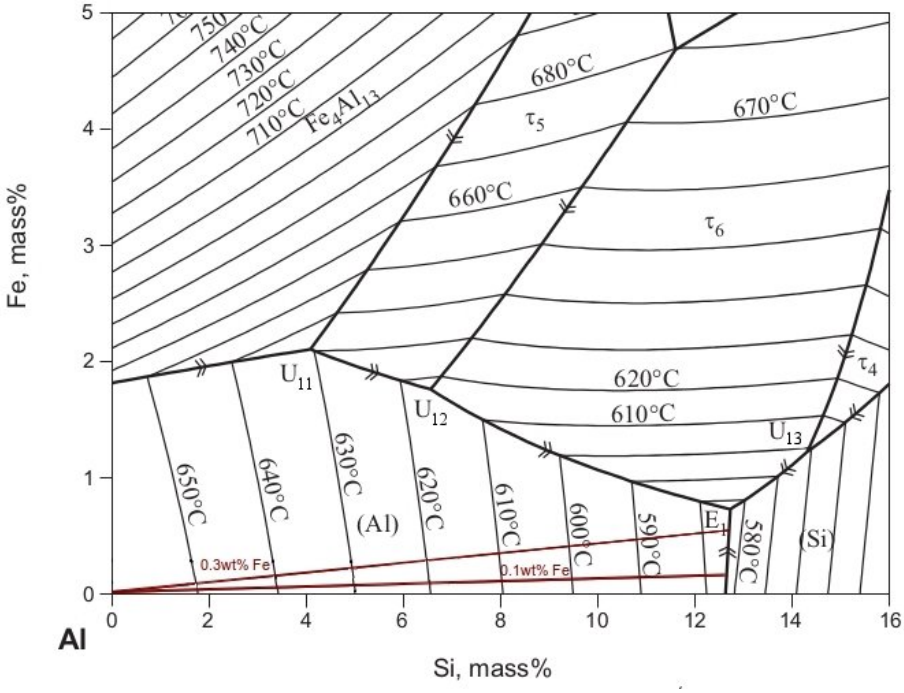

Figure 2.2: Liquidus projection of the ternary phase diagram for Al-Fe-Si in the Al-rich corner as given in [35] based on the work by Liu et al. [36]. τ_5 is α and τ_6 is the β. The reactions indicated have been corrected to match the numbering in Figure 2.1. The solidification path for 7wt% Si and 0.1 and 0.3wt% Fe is shown, predicting Al, Al + Si and finally the eutectic Al + Si + β

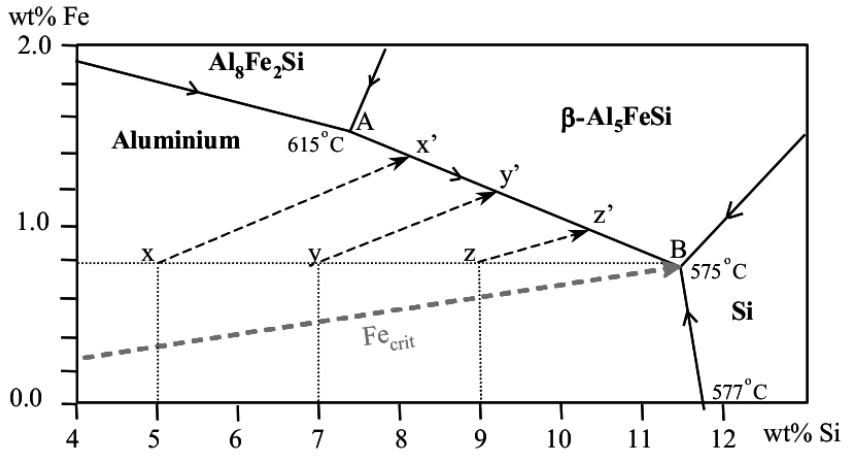

Figure 2.3: Ternary phase diagram for Al-Fe-Si in the Al-rich corner with superimposed solidification paths of Al based on Sheil assumptions for an iron content of 0.8wt%. Paths for 5wt% (x-x‘), 7wt% (y-y‘) and 9wt% (z-z‘) Si are shown. Fe_{crit} indicates the highest Fe-content that avoids the coarse binary eutectic β precipitation prior to the eutectic reaction. Reproduced from Taylor [4].

2.2 Alterations to the solidification path

2.2.1 The effect of Mn

The α-phase's ability to dissolve Mn was reported by Phillips and Varley [19] and the Mn-rich α-phase was later shown to be cubic [18, 25]. The ability of Mn to dissolve in the α-phase and stabilize it is widely accepted today [4, 21]. An example of reported Mn-levels in Fe-rich intermetallics is given in Table 2.1.

A new phase, still called α, is formed and its formulas are reported in various ways as e.g. $Al_{19}(Fe,Mn)_5Si_2$ [24, 21], $Al_{19}Fe_4MnSi_2$ [37] and $Al_{15}(Fe,Mn)_3Si_2$ [38, 4]. This Chinese script-like α-phase is more favourable than the needle-shaped β-phase, thus an addition of Mn may be beneficial for the alloy as it favours the formation of script over needles [5]. An example of how the phase boundaries change is seen by comparing Figures 2.4 and 2.5 where the β-area is seen to be displaced to higher Fe-levels upon Mn-additions [20]. It is also possible to counter this effect as Mg may stabilize the β-phase [20].

In the case of a Mn-free alloy, the equilibrium solidification would proceed according to the phase diagram in Figure 2.4. The α-area is bypassed for all the alloys containing higher Fe-concentrations and aluminium dendrites, β or Si (depending on Fe-concentration) and eutectic (Al + Si + β) are the different phases forming. The β would form (for the higher Fe-concentrations) in the binary eutectic Al + β before the main eutectic Al + Si + β. The binary reaction would lead to a larger volume fraction of β and these particles would be coarser than the eutectic ones as they would have a larger liquid space to grow in [20].

When Mn is added the α area is enlarged and the β area displaced to higher Fe-levels, as seen in Figure 2.5 for a 0.4wt% Mn addition. Binary α can form for the alloys with higher Fe-levels and a new ternary eutectic, Al + α + β, is suggested prior to the main eutectic reaction Al + Si + β (E_1 in Figures 2.1 and 2.2). The decrease in amount of binary eutectic β would cause less and finer β-needles as β mainly will form in eutectic reactions. The binary α forming will be coarser and the total amount of Fe-rich intermetallic particles have been shown to increase [22].

Indications of how the phase diagram gradually changes upon Mn-additions inbetween the diagrams shown in Figures 2.4 and 2.5 is shown in Figure 2.6 for 0.1wt% Mn (a) and 0.2wt% Mn (b). The α precipitation area is gradually seen to displace the β area.

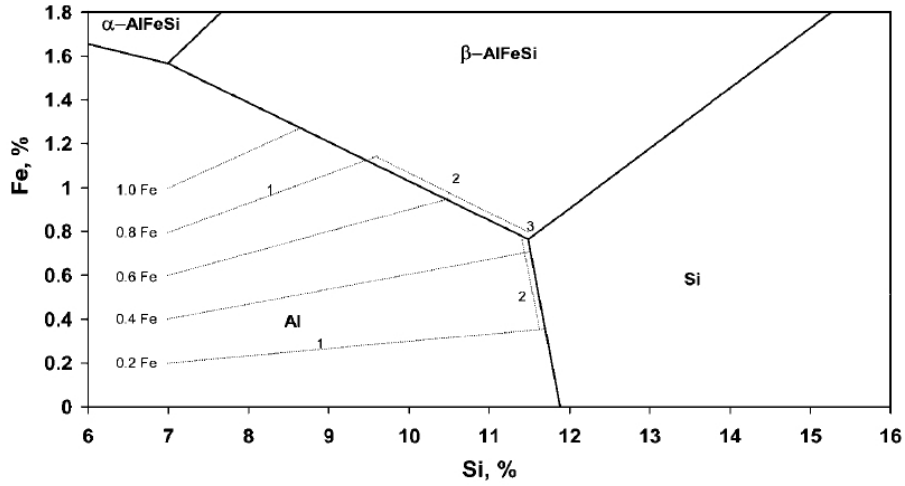

Figure 2.4: An example of a phase diagram for a Mn-free alloy with solidification paths for different Fe-contents using the Scheil equation (equation 2.1). The numbers indicate the different solidification steps, where 1 is primary Al, 2 is binary eutectic solidification (Al + β or Al + Si) and 3 is the ternary solidification of the main eutectic Al + Si + β (called E_1 in Figures 2.1 and 2.2) [20]

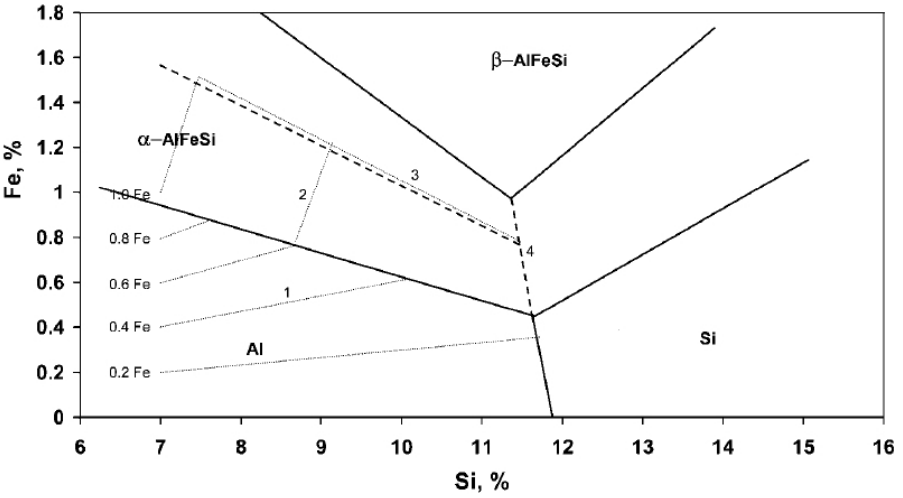

Figure 2.5: An example of a phase diagram showing the change upon addition of 0.4wt% Mn with solidification paths for different Fe-contents using Scheil's equation (equation 2.1). The numbers indicate the different solidification steps. For high Fe-levels (0.4-1.0wt%) 1 is primary Al dendrites, 2 is binary Al + α solidification , 3 is the ternary eutectic Al + α + β solidification and 4 is the ternary main eutectic Al + Si + β. The low Fe-level (0.2wt% Fe) would proceed through primary Al dendrites, binary eutectic Al-Si and finally the ternary Al + α + β eutectic [20]

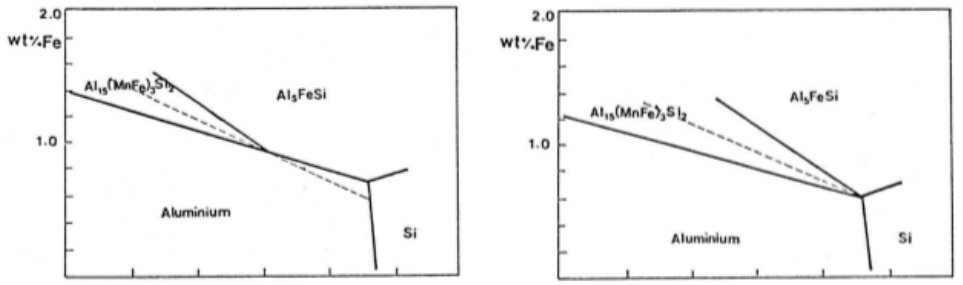

(a) **(b)**

Figure 2.6: Two phase diagrams for Mn-levels inbetween the two in Figures 2.4 and 2.5. (a) shows 0.1wt% and (b) 0.2wt% Mn. The α precipitation area is seen to gradually displace the β area. Reproduced from [7].

2.2.2 The effect of V

Though the stabilizing effect is mostly investigated for additions of Mn, it was shown by Munson [25] for a 6wt% Si and 2.5wt% Fe alloy that vanadium (and chromium) could cause the structure of the α-phase to change from hexagonal to cubic as well. The concentrations causing the cubic structure was 0.1wt% V.

The stabilization of α due to V was confirmed by Skinner et al. [26]. An analysis based on valence electron structure of the cubic α-phase was conducted by Wang et al. [28], explaining the stabilizing effect of V. It was calculated that V atoms can replace Fe atoms in the structure without causing structural alterations. Also, the stability of the phase is improved due to the changes in bond energies upon the atom exchange. If V substitutes for Fe in the structure the atomic Fe/Si-ratio in the phase would be expected to be reduced when V is added to an alloy and the Fe/V-ratio should increase.

2.2.3 The effect of cooling rate and nucleation

The cooling rate is known to have an effect on the relative amounts of α and β forming. At the normal cooling rates obtained when casting aluminium in sand or permanent moulds the β-phase is mainly obtained [8].

In a Mn-free alloy, the suppression of β at higher cooling rates may be associated with the temperature at which it starts to form. It has been found that the nucleation temperature of β decreases upon increased cooling rate, until it reaches the eutectic Si temperature. The residual liquid remaining after the main eutectic reaction is depleted in Si and favours the crystallization of α over β, as α contains less Si [8]. Less β would therefore be expected for a higher cooling rate in the Mn-free alloy. The total volume fraction of α and β would also decrease as a consequence of this as most of the intermetallic particles would form

in the main eutectic, and therefore become finer. This is e.g. reported by by Khalifa et al. [11] for a 6.32wt% Si alloy not containing Mn (nor V), where β prevailed at lower cooling rates (around 0.2 K/s). This low cooling rate also yielded coarser as well as a larger total volume fraction of iron rich intermetallic phases as compared to the higher cooling rates (10-15K/s).

If Mn is added, α and β form together in the ternary Al + α + β reaction after the binary Al + α and prior to the main eutectic reaction (cf. Figure 2.5). The amounts of α and β forming in this reaction depend on the cooling rate. If a low cooling rate is applied most of the Fe is consumed in the binary reaction forming α prior to the ternary reactions. For a higher cooling rate the binary reaction would proceeds faster, consuming less Fe, thus leaving more Fe for the formation of α and β in the ternary eutectic reaction. More β would therefore be expected upon a high cooling rate for a Mn containing alloy [8].

The cooling rate will also affect the size of the α-and β-particles. According to Verma et al. [10] for a AA6063 alloy (0.54wt% Si, 0.56wt% Mg, 0.2wt% Fe and 0.05wt% Mn), higher cooling rates (7.7 K/s) should cause the intermetallic particles to become smaller and shorter, as well as altering the morphology of the α-phase from a seaweed/petal shape towards a more dendrittic shape. For lower cooling rates the particles should become coarser, more interconnected and more extended. This is consistent with the suppression of binary eutectic β (and binary α if the α-phase is stabilized sufficiently) at higher cooling rates (higher growth velocities) and thus finer particles due to the ternary eutectic reactions. The eutectic itself would also become finer at higher cooling rates as there is a relationship between the growth velocity (V) and lamellar plate spacing (λ) shown in equation 2.2 [39].

Increased cooling rates have been found to promote heterogeneous nucleation of Fe-intermetallics onto various inclusions [40]. It has also been proposed that AlP, which is a potential nucleus for eutectic silicon, may aid the nucleation of the β-platelets [14], possibly through the (Al,P)O_2 phase [20]. In addition, TiB_2 particles, added for grain refinement in commercial alloys, have been observed to directly promote β-formation. It is suggested that if more TiB_2 particles than necessary for Al nucleation is added, some particles will remain inactive in the interdendrittic liquid and be available for β-nucleation [15]. The potent nuclei would lower the undercooling (ΔT) for the phases, thus causing a coarsening of the eutectic (larger λ) according to equation 2.3 [39].

$$\lambda^2 V = Constant \tag{2.2}$$

$$\Delta T \lambda^2 = Constant \tag{2.3}$$

2.3 Crystal structure and stoichiometry

In order to understand the parameters applied by the EBSD off-line *Orientation Imaging Microscopy* (OIM) analysis software [41], the crystallographic information for the Fe-rich intermetallic particles must be obtained.

2.3.1 The α-phase

α-AlFeSi is commonly accepted to be hexagonal [38, 42] and to have a stoichiometry of Al_8Fe_2Si [38], referred to as α_h. The Al(Fe,Mn)Si-phase is accepted to have a cubic structure [24, 25], referred to as α_C to distinguish it from the hexagonal phase. Since transition elements such as Mn may stabilize this alpha-phase, Munson et al. proposed that as the Mn/Fe-ratio in the alloy increases the structure of the α-AlFeSi will gradually change from hexagonal through body centred cubic to simple cubic [25]. An example of a study showing average Mn-content in script-like and needle-like intermetallic particles is given in Table 2.1.

The α-phase may also dissolve V. A study reporting V-levels in different Fe-rich intermetallic particles, measured by EPMA, is reproduced in Table 2.2. The stabilization of α by vanadium (0.59-1.47wt%) was confirmed by Skinner et al. [26], estimating the stoichiometry to be $Al_{12}(Fe,V)_3Si$. The same stoichiometry has been shown by Coelho et al. [43] in a mechanically alloyed aluminium alloy. Maitland et al. [44] also confirmed a cubic α-(AlFeSi) phase in V-containing wrought Al-alloys. This study reported more cubic α after homogenization. Rodriguez and Skinner [27] extracted and analysed dispersoids from two melt spun alloys of composition 8.3 and 8.6wt% Fe, 0.8 and 1.92wt% V and 1.75 and 2.42wt% Si. Two cubic phases called α_{12} and α_{13} were found and are given in Table 2.3. This table gives a summary of crystallographic information on the different α- and β-phases as well.

2.3.2 The β-phase

The β-AlFeSi phase is commonly described as Al_5FeSi [45] or $Al_{4.5}FeSi$ [46], however, other variations in stoichiometry have also been reported.

The crystal structure of β-AlFeSi is still not fully agreed upon. The two main possibilities are monoclinic and orthorhombic. The problem related to deciding the crystal structure is determining the β-angle in the structure. It is reported in the range 90-91°, where 90° suggests orthorombic and deviation from 90° suggests monoclinic. Also, a possible tetragonal structure due to similar length of *a* and *b* (in combination with a 90° β-angle) [47] has been suggested.

Rømming et al. [46] attempted to determine the crystal structure by a combination of X-ray and electron diffraction on crystals grown in a melt. They deduced a monoclinic structure, as given in Table 2.3. The work was revisited by Hansen et al. [47] due to the poor quality of the crystals in the primary work. This work used synchrotron powder diffraction as well and showed that the half unit cell had a structure closer to the tetragonal unit cell, also given in Table 2.3.

Mn may accumulate in β as well as α, however in far lower concentrations. An example of a study showing average Mn-content in Chinese script-like and needle-like intermetallic particles is given in Table 2.1. An Al_5(Fe,Mn)Si phase has been suggested [22, 23], but EBSD analysis of Mn containing β-particles have shown agreement with a tetragonal Al_3(Fe,Mn)Si_2 structure [24] more commonly designated δ-phase [21].

The β phase may also dissolve V. Reported V-levels in different Fe-rich intermetallic particles are reproduced in Table 2.2, where one phase has stoichiometry resembling the β-Al_5FeSi.

Table 2.1: Example of average Mn-content in Fe-rich intermetallic phases in a cast Al-alloy, measured by EPMA. The alloy contained 7wt% Si and 0.4wt% Mg [22].

Alloy		Particle			
Fe [wt%]	Mn [wt%]	Particle type	Fe [wt%]	Mn [wt%]	Fe/Mn-ratio (atomic)
0.7	0	Needle-like	26.01	0.01	-
0.7	0.3	Needle-like	20.76	3.88	4.70
0.7	0.3	Needle-like	20.58	3.36	5.38
0.7	0.3	Script-like	21.02	8.36	2.23
0.7	0.3	Script-like	21.10	8.49	2.18

Table 2.2: Reported V-content in Fe-rich intermetallic phases measured by EDX microanalysis. The two alloys contained 0.9 and 1.7wt% Si [29].

Alloy			Particle		
Fe [wt%]	V [wt%]	Cooling rate [K/s]	2D morphology	V [wt%]	Suggested composition
8.3	0.8	14	Star shaped	1.2	$Al_{13}(FeVSi)_4$
8.3	0.8	1	Six-armed rod	1.4	$Al_{13}(FeVSi)_4$
8.3	0.8	1	Rod shaped	0.8	$Al_{13}(FeVSi)_4$
8.3	0.8	1	Needle shaped	0.2	$Al_5Fe(VSi)$
8.6	0.8	14	Degenerate star	0.8	$Al_5Fe(VSi)$
8.6	0.8	14	Elongated β	0.2	Al_5FeSi

Table 2.3: Reported crystallographic information on the two intermetallic phases α-and β-AlFeSi. Explanations for the space group symbols can be found in Appendix B.

Phase [Reference]	Crystal structure	Cell parameters [nm]	Space group
Al [48]	Cubic	$a = 0.40488$	$Fd\bar{3}m$
Si [48]	Cubic	$a = 0.54286$	$Fm\bar{3}m$
α_h-Al_8Fe_2Si [49]	Hexagonal	$a = 1.240$	$P6_3/mmc$ [48]
		$c = 2.623$	
α_c-$Al_{19}(FeMn)_5Si_2$ [24]	Cubic	$a = 1.256$	$Im\bar{3}$
α_{13}-$Al_{13.37}(FeV)_{3.0}Si_{1.11}$ [27]	Cubic	-	Im3
α_{12}-$Al_{12.86}(FeV)_{3.0}Si_{2.1}$ [27]	Cubic	-	Pm3
β-$Al_{4.5}FeSi$ [45]	Orthorhombic	$a = 0.618$	Cmcm
		$b = 0.620$	
		$c = 2.08$	
		$\beta = 90°$	
β-$Al_{4.5}FeSi$ [46]	Monoclinic	$a = 0.616$	A2/a,
		$b = 0.617$	C2/c [48]
		$c = 2.08$	
		$\beta = 90.42°$	
β-$Al_{4.5}FeSi$ [47]	Tetragonal	$a = b = 0.616$	4m
		$c = 1.04$	
		$\beta = 90°$	

2.4 SEM - Energy Dispersive Spectrometry (EDS)

Upon interaction between primary electrons generated by the electron gun in the SEM and an atom, an electron can be knocked out of its orbit. When an electron from a higher orbital falls into the newly created vacant position x-ray energy is emitted as photons or *Augerelectrons*. The energy of the different transitions between orbitals in different atoms is discrete. A transition from L- (quantum number, n=2) to K- (n=1) orbital causes a K_α-photon to be emitted. M- (n=3) to K-orbital (n=1) transition causes a K_β-photon to be emitted, and so forth. Similarly, transitions from higher orbitals to the L-orbital (n=2) leads to L-photons to be emitted. The element(s) present can thus be determined as there exits a relation between the atomic number and the energy of the primary electrons [50]. The K_α series was used in the current investigation.

By using computer software the analysis of EDS-spectra can be done relatively efficient. There is, however, the need for some corrections in order to do a quantitative analysis.

2.4.1 ZAF-correction

ZAF-corrections refers to corrections for atomic number (Z), absorption (A) and fluorescence (F) [50].

The atomic number correction (Z) is related to the average atomic number of the sample in question. It corrects for backscattered electrons, electrons that does not cause ionization of atoms and thus not emission of photons. Since the known number of primary electrons that are incident (based on the acceleration voltage) is related to the total number of photons registered, the backscattered electrons should be corrected for. Also, the deceleration of primary electrons and thus reduction in primary electrons will affect the ionization ability of the electrons. This is also corrected for by the Z-factor [51].

The absorption correction (A) is related to the point at which the photons are generated. The interaction may occur both at the surface and at some depth in the sample. Some photons may be absorbed or loose energy on its way out of the sample due to interaction with other atoms [50]. This self-absorption effect may cause a complicated relation between the composition and detected x-ray intensities that needs to be corrected for [51].

The fluorescence correction (F) is needed when the x-ray energy emitted from one element is sufficient to excite a different element on its way out of the sample. This will cause a mismatch between the measured and actual composition of the sample [50].

2.4.2 Background correction

When the primary electrons are approaching the surface of the sample, the electric field caused by the atoms will decelerate the electrons. This deceleration causes the electrons to loose some of their energy and give disturbances in the EDS-spectrum. A continuous background spectra will thus form, called *bremsstrahlung*. This background can be calculated by the EDS software, in this case Quantax EDS [52]. Both a physical and a mathematical model can be chosen.

It is necessary to determine the background, as the quantification algorithm uses the peak-to-background (P/B) ratios. This gives the possibility to obtain a standard less quantitative analysis based on the obtained spectrum alone [51].

2.5 SEM - Electron Backscatter Diffraction (EBSD)

In electron backscatter diffraction (EBSD) the sample is tilted to 70° to the horizontal in the SEM. The primary electrons interact with the crystal structure of the phase(s) on the sample's surface and are diffracted according to Braggs law due to crystal planes. The diffracted electrons are imaged on a phosphor screen and/or a camera where they give rise to bands in a *Kikutchi pattern*. This pattern represents the crystal structure and can be used for phase identification [50].

2.5.1 Off-line analysis

The off-line analysis program uses pre-set phases from a database. Both the hexagonal α-phase and the monoclinic β-phase were found in the database at hand. An overview of the parameters programmed in the database for the two intermetallics is given in Table 2.4.

Phase identification by indexing EBSD-patterns is done by comparing the obtained pattern with the pattern in the computer software's database. How well the obtained pattern matches the software's pattern is quantified by a *confidence index* (CI) with a number between 0 and 1, where 0 would be no match and 1 would be perfect match [53].

It has been shown that for an fcc crystal structure (in steel) the suggested indexing solution will be correct in 95% of the time when $CI > 0.1$ [54]. If a CI is obtained that is much larger than 0.1, the indexing could therefore be regarded as successful and the correct phase assumed to be found.

Table 2.4: The information found in the database for indexing diffraction patterns from EBSD by the OIM DC software [41]. These parameters can be compared with those found in the literature and shown in Table 2.3.

Phase	Crystal structure	Cell parameters [nm]	Point group
α-Al_8Fe_2Si	Hexagonal	$a = 1.2406$	$6/mmm$
		$c = 2.6236$	
β-$Al_{4.5}FeSi$	Monoclinic	$a = 0.6168$	$2/m$
		$b = 0.6166$	
		$c = 2.0809$	
		$\beta = 91.001°$	

Chapter 3

Experimental method

3.1 Alloy preparation

The alloys were prepared from high purity aluminium (5N: 99.999%) which was alloyed with 7wt% solar grade silicon (>6N: >99.9999 %). The compositional analysis provided from the suppliers is attached in Appendix C and D respectively. The Al pieces were cleaned by etching in ∼17% HCl for about 24 hours.

Ten Al-7Si alloys were made, with varying amounts of iron and vanadium. Two different cooling rates were also applied. The nomimal additions of Fe and V are given in Table 3.1. Fe and V were added as Al-5wt%Fe and Al-10wt%V master alloys, respectively. The grain refiner was added as a Al-5wt%Ti-1wt%B master alloy. The amounts of these master alloys were calculated based on the amount of Al used. The calculations can be found in Appendix E, along with the actual amounts. The master alloy pieces were cleaned in an ultrasonic bath with water for approximately 5 minutes.

The total melt mass was between 550 and 600 grams for each alloy. The alloys were prepared in preheated clay-graphite crucibles coated with Fibrefrax and Boron Nitride. The furnaces were set at 750°C. Before any interaction with the melt, such as master alloy addition or temperature measurement, the melt surface was skimmed with a graphite rod. The alloying elements and master alloys were preheated in a separate furnace for up to a couple of minutes before added to the melt. The alloyed melt was stirred and left for at least 30 minutes to ensure that the master alloys were fully dissolved.

Table 3.1: Nominal additions of impurity elements Fe and V and the cooling rate of the different alloys. The cooling rates are deduced from the cooling curves presented in Figure 3.1.

	Cooling Rate [K/s]	Fe-content [wt%]	V-content	Other
Alloy 1	0.9	0.1	0	
Alloy 2	0.9	0.3	0	
Alloy 5	0.9	0.1	600 ppm	
Alloy 6	0.9	0.3	600 ppm	
Alloy 3	0.9	0.1	0.2 wt%	
Alloy 4	0.9	0.3	0.2 wt%	
Alloy 7	0.3	0.3	0	
Alloy 8	0.3	0.3	600 ppm	
Alloy 9	0.3	0.3	0.2 wt%	
Alloy 10	0.3	0.3	0.2 wt%	Al-5Ti-1B (1g/kg alloy)

3.2 Casting

Small graphite crucibles with an outer diameter of 50 mm, an inner diameter of 30 mm and a height of 50 mm were used. The crucibles were preheated until they were glowing red, for approximately 15 minutes, at 750°C before interacting with the melt. The melt temperature was controlled, always at 742°C $\pm$ 2 K prior to casting. The top of the melt was skimmed, the melt stirred and the crucibles placed on the melt surface for 1 minute. The crucible was then submerged to extract a sample. The crucibles were covered with a fiberfrax insulating lid. One disk for chemical analysis was cast for each alloy as well.

Two different cooling rates were employed. The cooling rate obtained for cooling in air with preheated crucible was 0.9 K/s and cooling with an insulated crucible gave 0.3 K/s. A commercial A356 alloy was used for testing the cooling rates. The curves for insulated and uninsulated crucibles are shown in Figure 3.1.

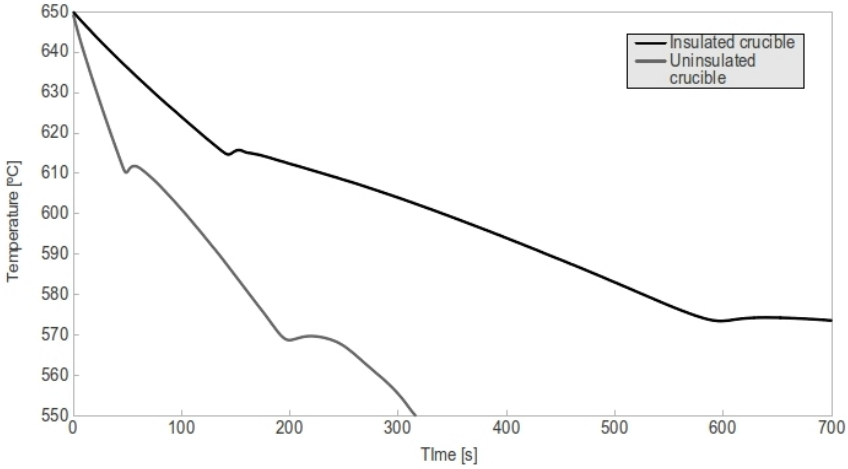

Figure 3.1: The cooling curve obtained logging the temperature in a commercial A356 alloy during solidification in a graphite crucible. A derivation of the cooling rate of the melt prior to any solidification reactions (between 650 and 620°C) gave a cooling rate of 0.9 K/s for the uninsulated crucible (grey line) and 0.3 K/s for the insulated crucible.

3.3 Sample preparation

Two samples from each alloy were initially prepared for analysis. The samples were cut through the middle either vertically or horizontally. They were cast in *ClaroCit* acrylic cold mounting resin when necessary to fit into holder for grinding and/or polishing. The samples were ground on SiC paper 320 with 15N force for 50 seconds. The samples were then polished on MD-Largo (6μm) at 20 N force for 5,5 minutes, MD-Mol (3μm) at 20 N for 3 minutes. The samples for secondary electron imaging and EDS were finally chemically polished with OP-Chem (1μm) and OP-S solution at 15 N for 2 minutes.

3.3.1 EBSD preparation

Two methods for sample preparation for the EBSD analysis were attempted. The first method was ion milling on a Hitachi Ion Mill. The second method was by exchanging the final OP-S polishing with an alumina suspension (OP-AN, 0.02μm). The ion milling proved not to be a good preparation technique for EBSD of the Fe-rich intermetallics. Some details and results on this method is provided in Appendix F. The samples prepared with alumina suspension were, after polishing down to 3μm, polished manually on MD-Nap with 0.25μm diamond paste for 2 minutes. Finally they were polished on OP-Chem with OP-AN (0.02μm) suspension at 15N for 2 minutes. With this preparation method very good EBSD-patterns of the intermetallic particles were obtained.

3.3.2 Deep etching

One sample from each of the 0.3wt% Fe samples were deep etched. The samples were ground on 80, 120, 320, 500, 800 and 1000 SiC paper with water and finally on 1200 SiC paper with ethanol. A solution of 10g iodine per 100mL methanol [55, 56] was prepared by stirring for approximately 10 minutes, until the iodine had dissolved. The samples were mounted face down in a beaker with the solution. A magnetic stirrer was applied and set on the lowest possible stirring rate. The beaker was covered with a plastic film. The samples were etched for 4 hours.

3.4 Sample analysis

3.4.1 Alloy chemical analysis

The sample disks cast for all the alloys were sent to Hydro Aluminium AS for chemical analysis. The analysis was done by optical emission spectroscopy (OES) and controlled against X-ray fluorescence (XRF) analysis.

3.4.2 SEM

Several low magnification secondary electron images (SE-images) were obtained in a Hitachi SU-6600 Scanning Electron Microscope (SEM) to investigate particle distribution in the microstructure. To analyse particles in the microstructure and determine their chemical composition, Energy Dispersive Spectrometry (EDS) was used. The information was analysed off-line on *Quantax Espirit* [52] with Peak-to-background (P/B)-ZAF correction and a physical model for background correction to obtain quantitative data.

Electron BackScatter Diffraction (EBSD) was also conducted in the SEM. The sample was tilted to 70°C with respect to the horizontal and EBSD-patterns aquired with the *NORDIF* software [57]. Diffraction patterns were acquired from the particles and indexed offline on *Orientation Imaging Microscopy DC* [41].

3.4.3 Particle quantification by area

Secondary electron images of the microstructure were analysed with *Image Access* [58]. The image was first calibrated by using the scale bar in the image. By defining and adjusting the roundness factor and minimum diameter, the software could distinguish needle-shaped (low roundness) and more rounded Chinese script-like (high roundness) particles. Some manual adjustments had to be made. The software output included the size of each discrete particle in μm^2, based on calibration of pixels based on the scale bar. Examples of analysis of script-like particles and needle-like particles are shown in Figures 3.2 and 3.3 respectively.

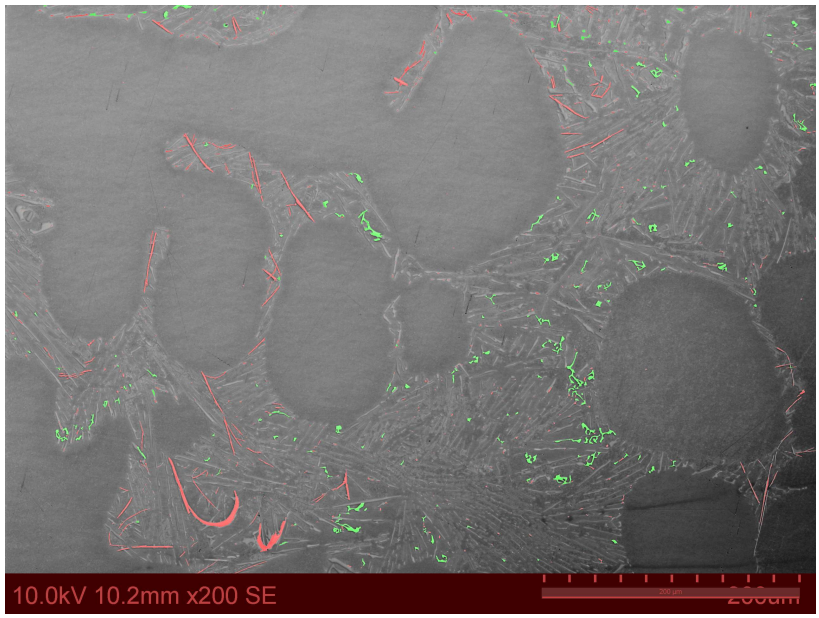

Figure 3.2: Example of quantification of Chinese script-like particles, the green indicates the particles selected for analysis. The roundness was in this case set to $>15\%$ and the minimum diameter to $>1\mu$m and some manual adjustments were made.

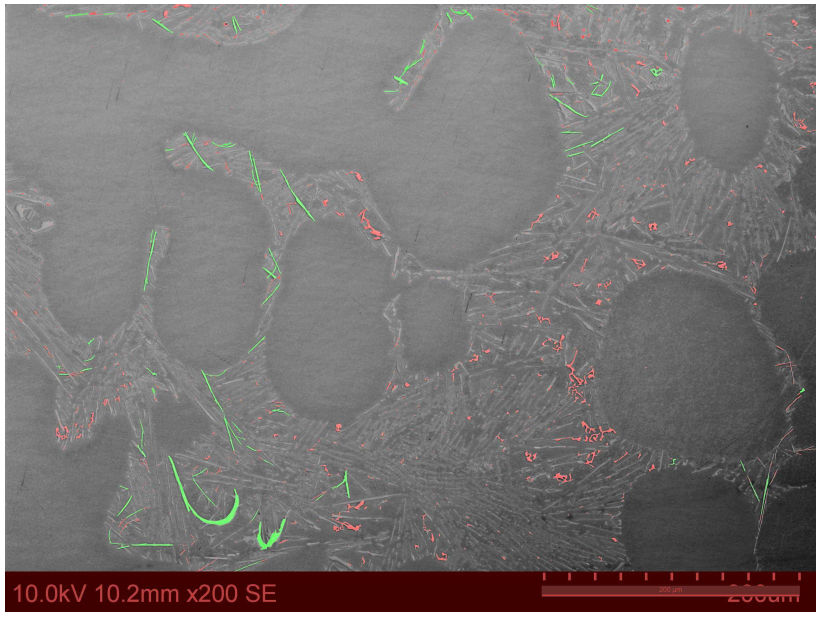

Figure 3.3: Example of quantification of needle-like particles, the green indicates the particles selected for analysis. The roundness was in this case set to $<15\%$ and the minimum diameter to $>1\mu$m and some manual adjustments were made.

Chapter 4

Results

4.1 Computer simulation: Alstruc

A prediction of the type and fraction of intermetallic particles was performed by the Alstruc software [59]. This software focuses on the Al-rich corner of the AlCuFeMgMnSi phase diagram. It takes into account solid-state diffusion and particle growth undercoolings. The composition and cooling rate are the input values and the software returns the temperature vs. fraction solid. It also provides other important information as output, e.g. the type, volume fraction and size of intermetallic particles [60].

Based on the composition and cooling rate, predicted amounts (volume%) of α and β intermetallic particles were calculated. The results are given in Table 4.1 below. The V-content was set to 0 as the effect of V on the Fe-rich intermetallic particles is not part of the software and therefore cannot be predicted.

Based on the analysis only β is predicted for both Fe-contents and both cooling rates. The amount of β increases with higher Fe-content but the two different cooling rates yields the same outcome.

Table 4.1: The input and results from the Alstruc simulation of the solidification path for the two different Fe-concentrations and the two cooling rates investigated.

Fe	Si	V	Cooling Rate [K/s]	Amount β [Volume%]	Amount α [Volume%]
0.1	7.0	0	1.0	0.264	0.0
0.3	7.0	0	1.0	0.825	0.0
0.3	7.0	0	0.3	0.825	0.0

4.2 Alloy composition analysis

Sample disks of each alloy were cast and sent to Hydro Aluminium AS for optical emission spectroscopy (OES) and X-ray fluorescence spectroscopy (XRF) analysis. The full results can be found in Appendix G and the average is given in Table 4.2 below. The actual compositions of the alloys are found to be very close to the nominal additions and are very consistent.

The chemical analysis for alloys 7-10 were not finished at the when this report was due. Based on the analysis for alloys 1-6, the last alloys would be expected to have a composition close to the nominal additions as well.

Table 4.2: A comparison of the calculated composition of the alloys and the average values obtained by OES and XRF analysis at Hydro. Alloy 10 is identical to alloy 9 except for the added grain refiner (TiB_2). The actual compositions are in good agreement with the nominal compositions. Analysis for alloys 7-10 was not finished at the time of submission of this report, but is expected to be in good agreement with the nominal additions as well.

	Nominal composition [wt%]			Actual composition [wt%]		
	Si	Fe	V	Si	Fe	V
Alloy 1	7.00	0.10	0.00	6.90	0.09	0.00
Alloy 2	7.00	0.30	0.00	6.88	0.26	0.00
Alloy 5	7.00	0.10	0.06	6.85	0.09	0.05
Alloy 6	7.00	0.30	0.06	6.84	0.26	0.05
Alloy 3	7.00	0.10	0.20	6.78	0.09	0.17
Alloy 4	7.00	0.30	0.20	6.82	0.26	0.17
Alloy 7	7.00	0.30	0			
Alloy 8	7.00	0.30	0.06			
Alloy 9	7.00	0.30	0.20			
Alloy 10	7.00	0.30	0.20			

4.3 Micrographs

4.3.1 High cooling rate - 0.9 K/s

Secondary electron (SE) micrographs of high cooling rate alloys follow. The white particles are Fe-rich intermetallic particles, the light grey needles are eutectic Si and the homogeneous grey areas are aluminium dendrites.

Figure 4.1 shows a micrograph of the 0.9 K/s, 0.1wt% Fe and 0 V alloy. In all the high cooling rate and 0.1wt% Fe alloys only Chinese script-like intermetallic particles were observed and they were small. There appear to be fewer Fe-rich intermetallic particles compared to the alloys with higher Fe-content.

Figures 4.2, 4.3 and 4.4 show micrographs of the 0.9 K/s and 0.3wt% Fe alloys in order of increasing V-content. The Fe-rich Chinese script-like intermetallic particles are seen to be small in these alloys as well. In the 0.2wt% V alloy (Figure 4.4) the script appear coarser as compared to the 600ppm V alloy (Figure 4.3). The needles also seem to become larger.

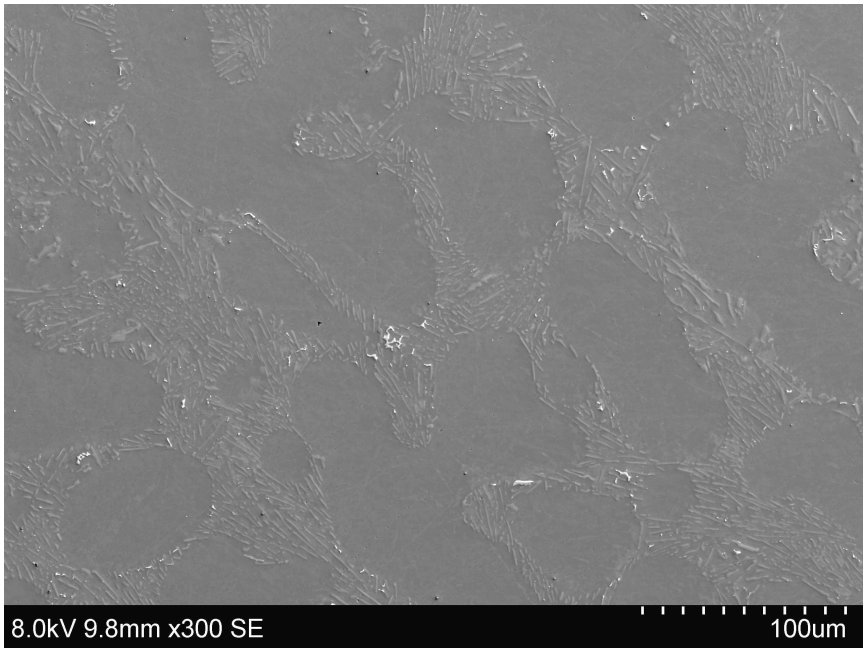

Figure 4.1: A SE micrograph of one of the high cooling rate and 0.1wt% Fe alloys, here represented by the 0 V alloy. All the Fe-rich intermetallic particles (white) observed in these alloys were Chinese script-like and no needle-like particles were observed.

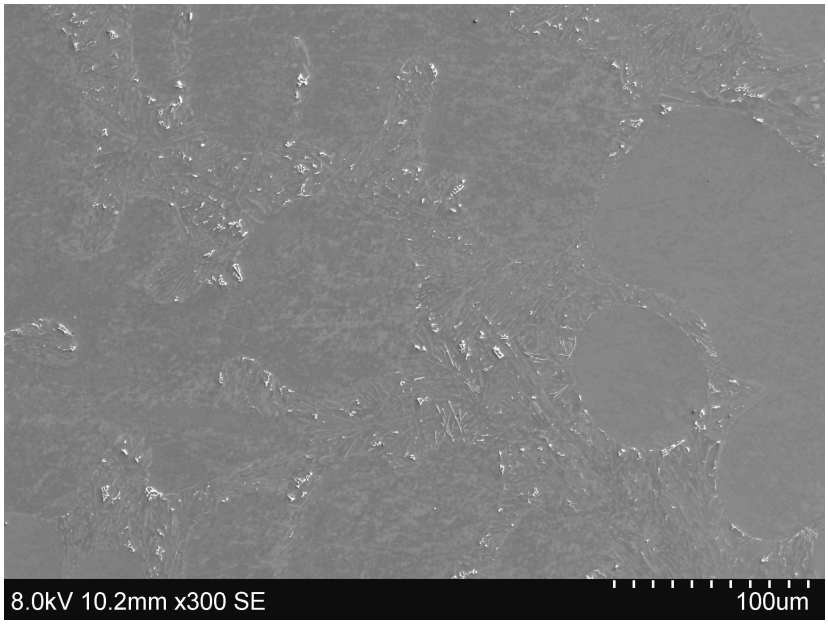

Figure 4.2: A SE micrograph of the high cooling rate, 0.3wt% Fe and no V alloy. Many small Chinese script-like Fe-rich intermetallic particles are seen and small colonies of needle-like particles can be found close to the centre of the image, down to the right.

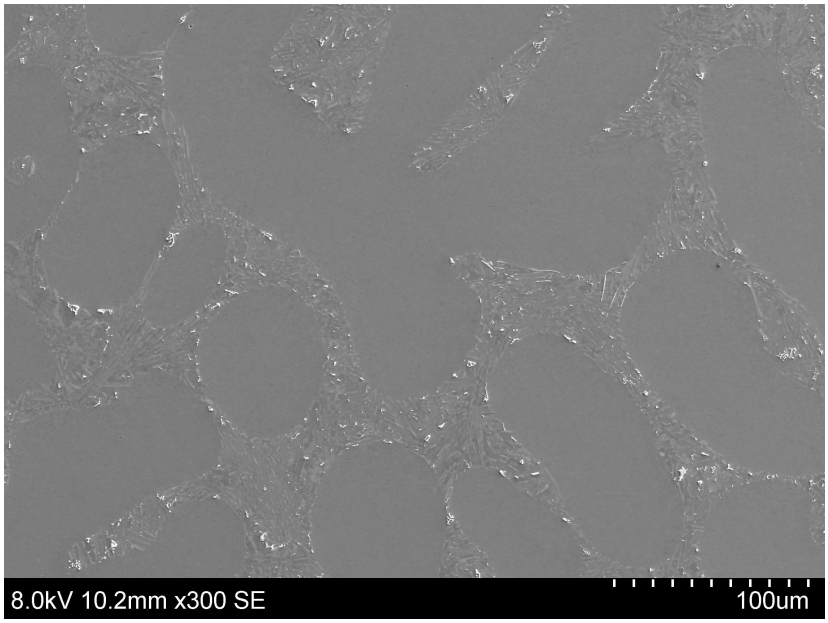

Figure 4.3: A SE micrograph of the high cooling rate, 0.3wt% Fe and 600ppm V alloy. Small Chinese script-like Fe-rich intermetallic particles are seen and some needle-like particles can be found right of the centre of the image.

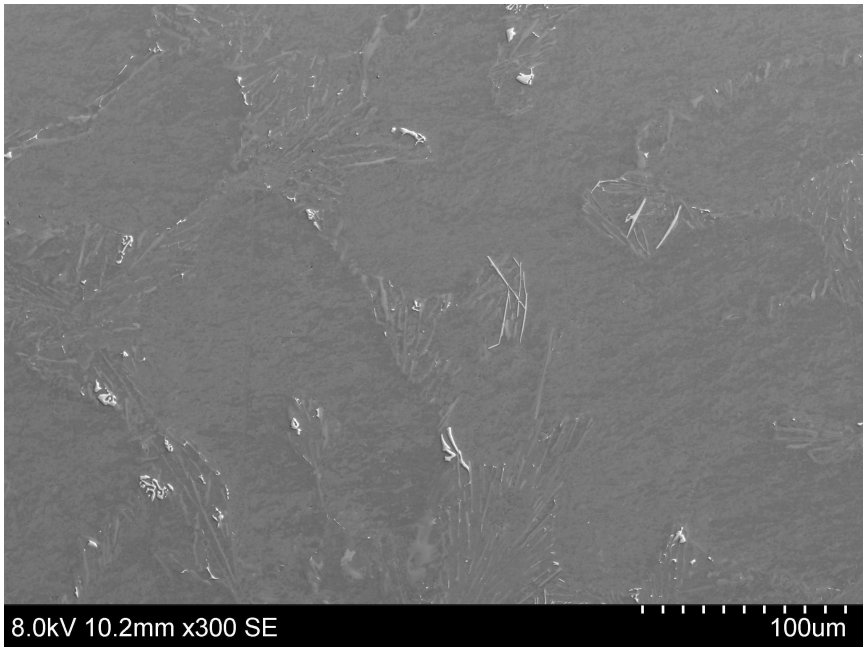

Figure 4.4: A SE micrograph of the high cooling rate, 0.3wt% Fe and 0.2wt% V alloy. The Chinese script-like Fe-rich intermetallic particles are fewer but larger compared to the alloys containing less V and the needle-like particles are also appear coarser.

4.3.2 Low cooling rate - 0.3 K/s

Secondary electron (SE) micrographs of low cooling rate alloys follow. The white particles are Fe-rich intermetallic particles, the light grey needles are eutectic Si and the homogeneous grey areas are aluminium dendrites.

Figures 4.5, 4.6 and 4.7 show micrographs of the 0.3wt% Fe alloys in order of increasing V-content. Both types of Fe-rich intermetallic particles are observed to be coarser than for the high cooling rate (0.9 K/s). More needle-like particles are also seen in the low cooling rate case as opposed to those alloys.

With increasing V-content more Chinese script-like particles are observed relative to the total amount of script- and needle-like particles. The needles are in majority for the lower V-contents, but script seem to prevail at the high V-content. The script appear to be coarser in the 600ppm V alloy than in the 0 V alloy. Both particles become finer and more fine script appears in addition to the larger script-like particles when the V-content increases from 600ppm V to 0.2wt%. Grain refiner (TiB_2) causes the number of needles to increase again and they seem to become coarser. This can be seen by comparing the micrographs of the two 0.2wt% V alloys in Figure 4.8 where (a) is without and (b) is with grain refiner.

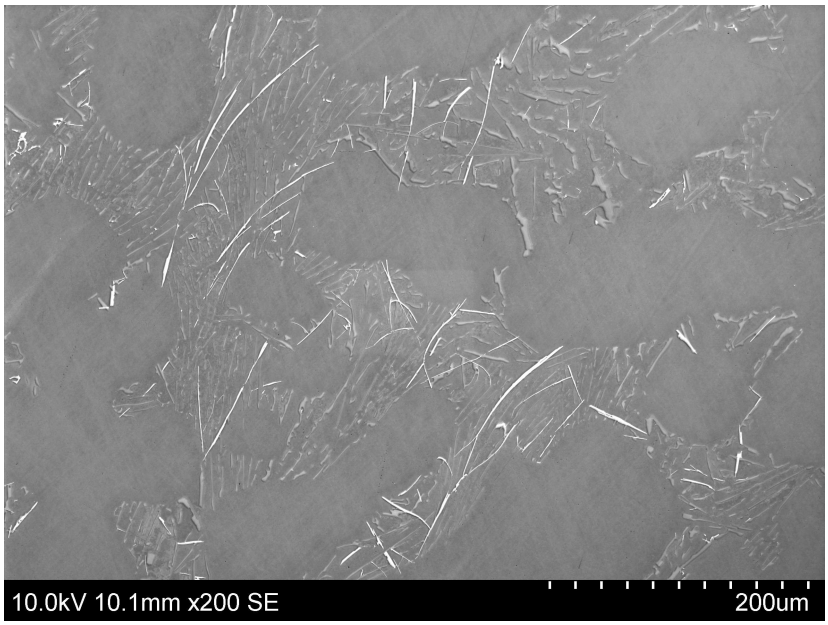

Figure 4.5: Representative SE micrograph of a 0.3wt% Fe and no V alloy. Both needle-like and Chinese script-like Fe-rich intermetallic particles are seen (white) and there seems to be more needle- than script-like particles.

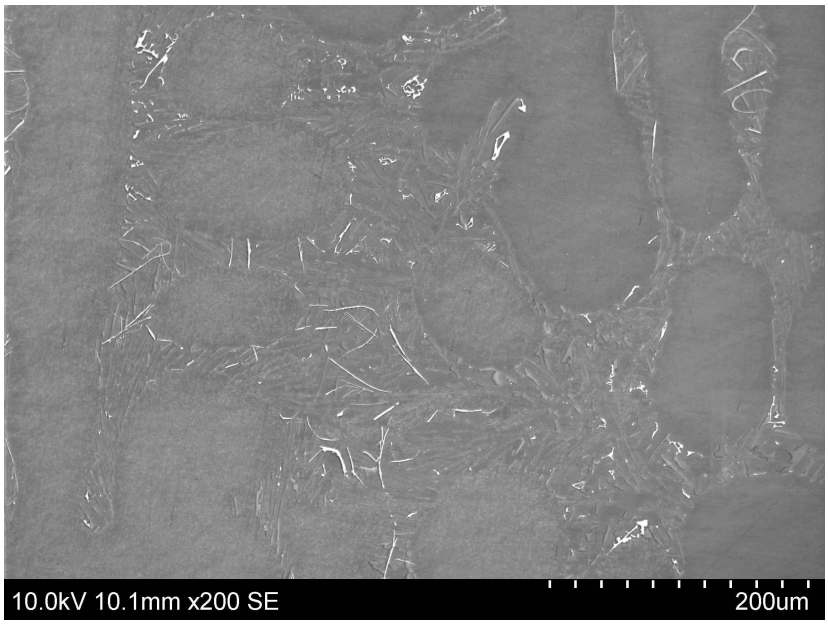

Figure 4.6: Representative SE micrograph of a 0.3wt% Fe and 600ppm V alloy. Both needle-like and Chinese script-like Fe-rich intermetallic particles are seen (white) and there seems to be more needle- than script-like particles.

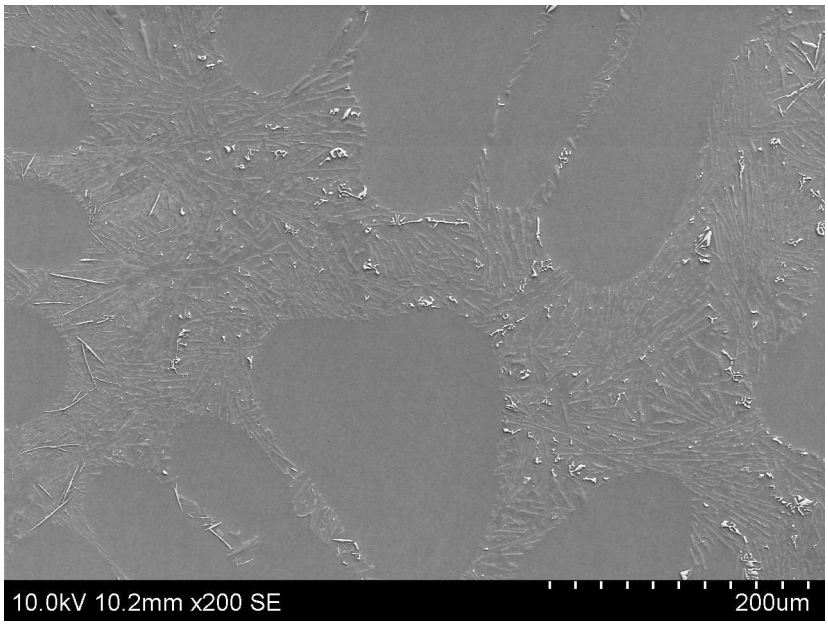

Figure 4.7: Representative SE micrograph of s 0.3wt% Fe and 0.2wt% V alloy. Both needle-like and Chinese script-like Fe-rich intermetallic particles are seen (white) and there seems to be far more script- than needle-like particles.

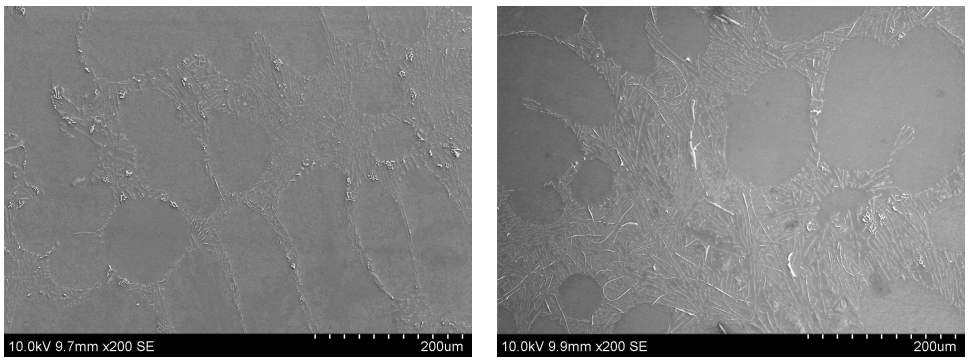

(a) **(b)**

Figure 4.8: SE images of 0.2wt% Fe alloys without (a) and with (b) grain refiner. There is far more needle-like intermetallic particles in the alloy with grain refiner than the one without and the needles appear to be larger when grain refiner is present.

4.4 Image analysis: Particle quantification by area

4.4.1 Relative amounts of Chinese script-and needle-like particles

Quantification of the two different particle shapes (Chinese script and needles), based on the area of the image was conducted with the Image Access software [58]. The software analysed particles based on roundness and minimum diameter. Low roundness (typically $<$15-20%) yielded needle-like particles and high roundness ($>$15-20%) script-like particles. The minimum diameter was set to $>1\mu m$ and manual adjustments to the selected particles were done. The calculation is based the number of pixels in the images, where the pixels were calibrated to the scale bar to yield μm^2.

Results giving the fraction of script-like intermetallic particles relative the total area of intermetallic particles are shown for the low and high cooling rates in Tables 4.3 and 4.4, respectively. Only the 0.3wt% Fe alloys were analysed as no needles were observed in high cooling rate and 0.1wt% Fe alloys. The average total area of both particle types for the low cooling rate are shown in Figure 4.9 and for the high cooling rate in Figure 4.10.

For low cooling rate the average area fraction of script-like particles, relative to the total area of needles and script, increases with increasing V-content (see Table 4.3). The average total area of particles decreases upon V additions (see Figure 4.9). By addition of grain refiner to the 0.2wt% V alloy, the average area of script-like particles decreases.

For high cooling rate the average total area fraction of script-like particles, relative to the total area of needles and script, is overall very high and appears to be decreasing upon increasing V-content (see Table 4.4). The average total area of particles increases from 0 to 600ppm V due to increases in area of both script and needles. From 600ppm to 0.2wt% V the total average area decreases due to a decrease in the area of script-like particles (see Figure 4.10).

The total area fraction of intermetallic particles, relative to the entire image was very low ($<$0.5%) for all the alloys. A table showing the total area fraction of script-and needle-like particles is shown in Appendix H.

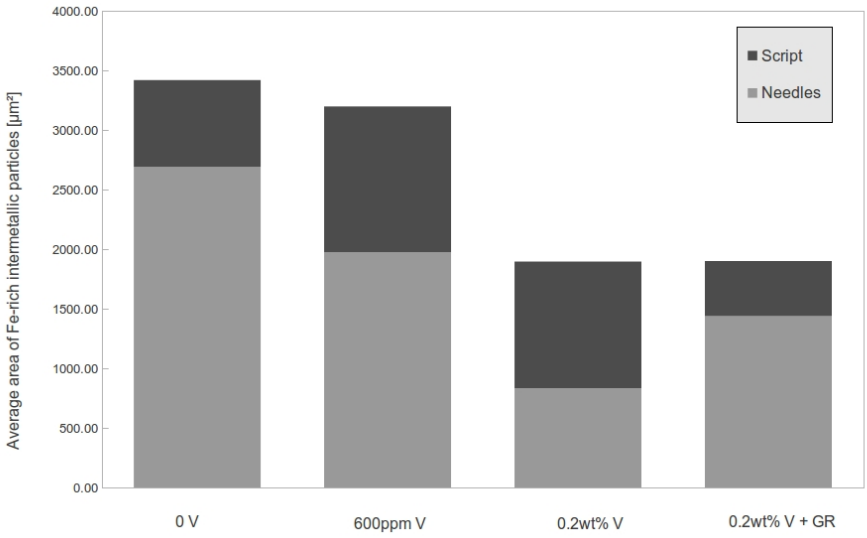

Figure 4.9: The average total area [μm^2] of Chinese script-like (dark grey) and needle-like (light grey) Fe-rich intermetallic particles in the low cooling rate alloys. The average total area of particles decrease with increasing V-content. The area of needles decreases with increasing V-content in the alloy and increases again by addition of grain refiner (GR) for the 0.2wt% V alloys.

Table 4.3: Analysis results of micrographs of the low cooling rate alloys giving the area fraction of Chinese script-like intermetallic particles relative to all intermetallic particles (script and needles). The average area fraction of script-like particles increases with increasing V-content. GR refers to grain refiner (TiB_2).

	Area fraction of particles that were Chinese script-like [%]						
Alloy	Image 1	Image 2	Image 3	Image 4	Image 5	Image 6	Average
0 V	6	12	9	26	19	65	23
600ppm V	17	22	30	36	41	50	33
0.2wt% V	80	31	31	42	76	62	54
0.2wt% V + GR	29	18	22	23	34	23	25

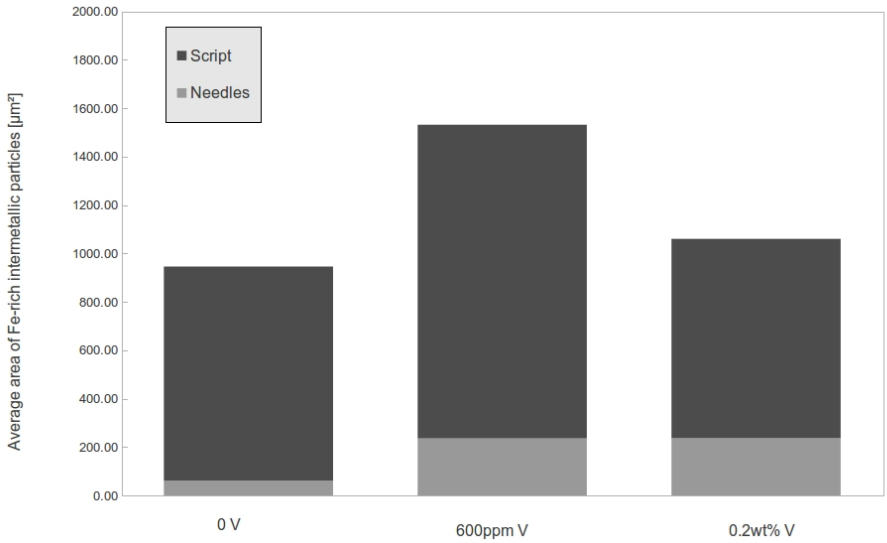

Figure 4.10: The average total area [μm^2] of Chinese script-like (dark grey) and needle-like (light grey) Fe-rich intermetallic particles in the high cooling rate alloys. The script-like particles make up the majority of particles and the average total area increases from 0 to 600ppm V due to a small increase in area of needles and a large increase in the area of script. Then the average total area decreases from 600ppm to 0.2wt% V due to a decrease in the area of script-like particles.

Table 4.4: Analysis results of micrographs of the high cooling rate alloys giving the area fraction of Chinese script-like intermetallic particles relative to all intermetallic particles (script and needles). The average area fraction of script-like particles are overall very high.

	Area fraction of particles that were Chinese script-like [%]					
Alloy	Image 1	Image 2	Image 3	Image 4	Image 5	Average
0 V	99	92	86	97	98	94
600ppm V	100	94	96	51	91	86
0.2wt% V	98	46	98	78	79	80

4.4.2 Particle size distributions

Figures 4.11 and 4.12 show the particle size distributions for Chinese script-like intermetallic particles in the low and high cooling rate alloys respectively. Figures 4.13 and 4.14 show the particle size distributions for needle-like intermetallic particles likewise. The overall trend is a decrease in area fraction upon increasing size.

All particles $<5\mu m^2$ has been discarded. In the case of Chinese script-like particles, these might belong to larger (more elaborate) particles but appear discrete due the 2D cross section. In the case of very small needle-like particles the software has difficulties separating needle- and script-like particles, thus rendering their classification uncertain. The threshold size where the software started counting particles also varied somewhat causing a biased number of particles in the 0-5μm^2 class. Further, the number of small particles (0-5μm^2) is large in all four cases and a trend in sizes $>5\mu m^2$ is easier seen graphically if these values are omitted.

For the script-like particles there is less of the lowest size class in the 0.3 K/s alloys (Figure 4.11) than in the 0.9 K/s (Figure 4.12). The low cooling rate also contains particles of the larger size classes which are absent at the higher cooling rate, but the size classes 10-15, 15-20 and 20-25μm^2 contain about the same fraction of particles.

For the needle-like particles the trend is similar. The low cooling rate contains less particles in the lowest size class and in the larger size classes there are particles which are not present at the high cooling rate. The decrease in fraction of the different size classes is far more rapid in the high cooling rate alloys than the low cooling rate alloys.

By comparing script- against needle-like particles for the same cooling rate (Figure 4.11 against 4.13 and 4.12 against 4.14), needles appear to have a slightly larger fraction of the medium and large size classes than the script-like particles for the low cooling rates. This trend is not obvious for the high cooling rate.

The grain refined alloy is seen in Figure 4.11 for script-like particles and 4.13 for needle-like particles. In case of the script there does not seem to be any differences between the particle sizes in the grain refined and unrefined alloy. For the needles the grain refined alloy seem seems to contain particles of larger size, compared to the unrefined alloy.

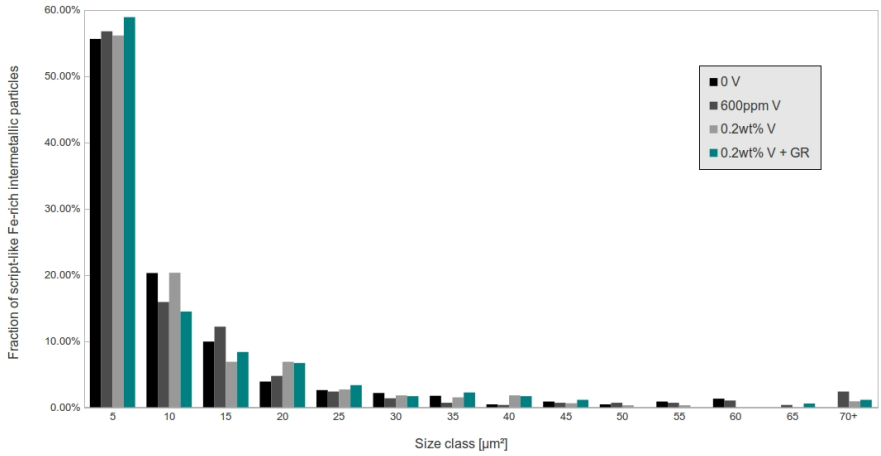

Figure 4.11: Percentage of Chinese script-like particles, relative to the total number of such particles with sizes larger than $5\mu m^2$, as a function of size classes in the low cooling rate alloys. The size classes are defined according to the particle areas where 5 refers to 5-10μm^2, 10 to 10-15μm^2, etc. The last class, called 70+, takes into account all particles $>70\mu m^2$. GR stands for grain refiner. There are decreasing amounts with increasing particle sizes and the alloy added grain refiner doesn't differ much from the corresponding alloy without.

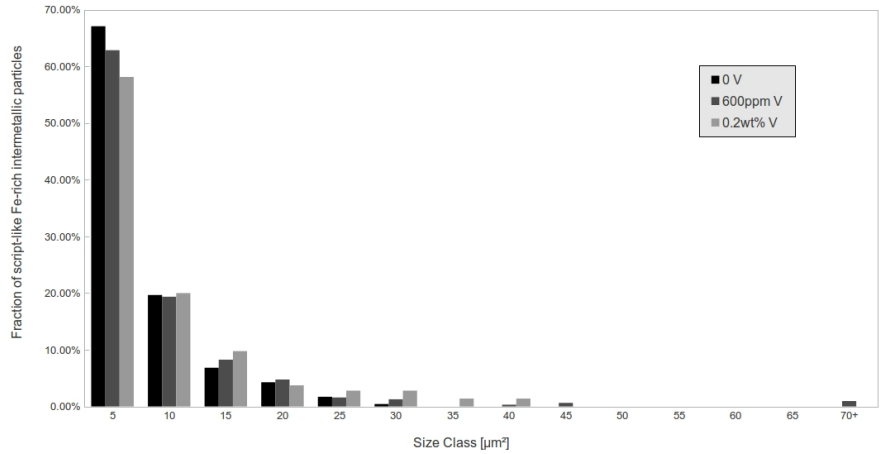

Figure 4.12: Percentage of Chinese script-like particles, relative to the total number of such particles with sizes larger than $5\mu m^2$, as a function of size classes in the high cooling rate alloys. The size classes are defined according to the particle areas where 5 refers to 5-10μm^2, 10 to 10-15μm^2, etc. The last class, called 70+, takes into account all particles $>70\mu m^2$. There are decreasing amounts with increasing particle size.

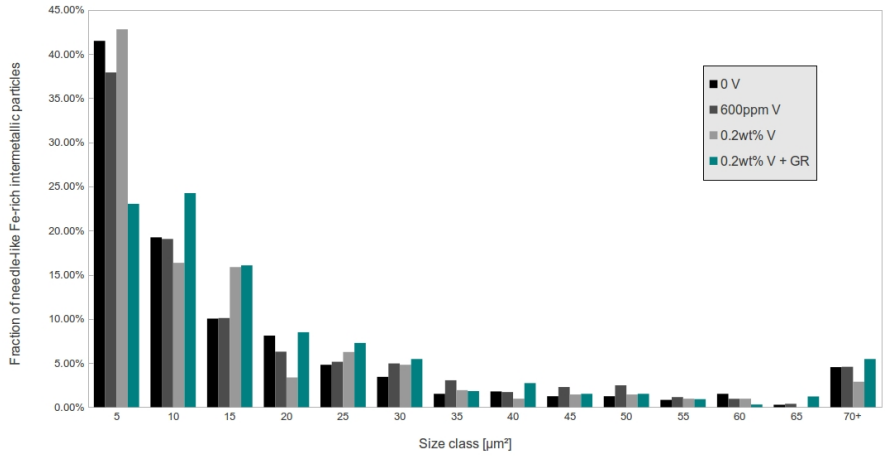

Figure 4.13: Percentage of needle-like particles, relative to the total number of such particles with sizes larger than $5\mu m^2$, as a function of size classes in the low cooling rate alloys. The size classes are defined according to the particle areas where 5 refers to 5-10μm^2, 10 to 10-15μm^2, etc. The last class, called 70+, takes into account all particles $>70\mu m^2$. GR stands for grain refiner. There are decreasing amounts with increasing particle size and the alloy added grain refiner seems to contain larger needles than the corresponding alloy without.

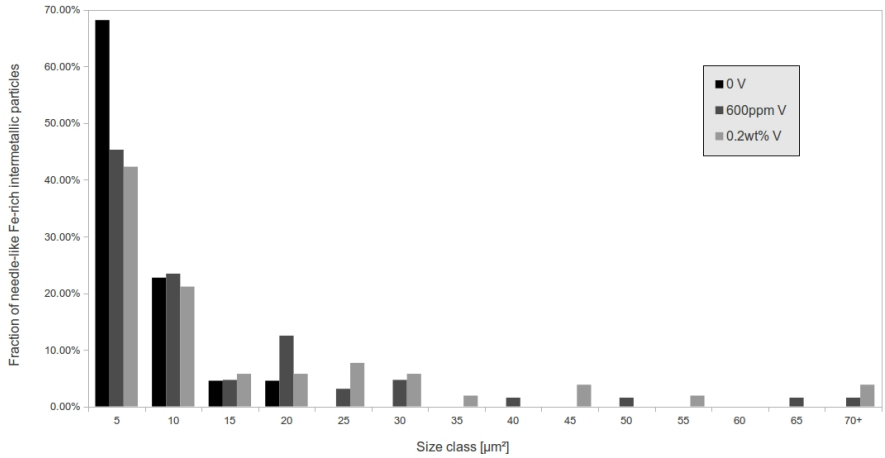

Figure 4.14: Percentage of needle-like particles, relative to the total number of such particles with sizes larger than $5\mu m^2$, as a function of size classes high cooling rate alloys. The size classes are defined according to the particle areas where 5 refers to 5-10μm^2, 10 to 10-15μm^2, etc. The last class, called 70+, takes into account all particles $>70\mu m^2$. There are decreasing amounts with increasing particle size.

4.5 SEM-EDS

4.5.1 V-content in Fe-rich intermetallic particles

Table 4.5 gives the average V-contents in both at% and wt% measured in the two types of Fe-rich intermetallic particles. The average V-content in the particles (wt%), with standard deviation, as a function of the V-content in the alloy is shown graphically for the Chinese script-like particles in Figure 4.15 and needle-like particles in Figure 4.16.

With increasing V-content in the alloys the average measured V-content in the script-like intermetallic particles increases. The grain refined alloy also seems to have script with a slightly higher V-content as compared to the alloy without grain refiner. The V-contents are larger for the alloys cast at the lower cooling rate compared to the higher cooling rate. The atomic Fe/V-ratio is also given for script-like particles in Table 4.5. The ratios are seen to be relatively high.

For the needle-like intermetallic particles the average V-content is very low. Some V is measured for the alloys containing 600ppm and 0.2wt% V but the standard deviations are large.

Table 4.5: Average V-content in Fe-rich intermetallic particles in the 0.3wt% V alloys. The values are based on several EDS measurement points on several particles in each alloy. The atomic Fe/V-ratio is also given for the Chinese script-like particles in alloys added V. GR refers to grain refiner (TiB_2).

	Script-like particles			Needle-like particles	
Alloy	V-content [wt%]	V-content [at%]	Fe/V-ratio	V-content [wt%]	V-content [at%]
High cooling rate (0.9 K/s)					
0V	0.0 ± 0.0	0.0 ± 0.0	-	0.0 ± 0.0	0.0 ± 0.0
600ppm V	0.4 ± 0.2	0.3 ± 0.1	76.8 ± 36.2	0.1 ± 0.1	0.0 ± 0.0
0.2wt% V	1.5 ± 0.8	1.0 ± 0.5	19.9 ± 10.4	0.2 ± 0.1	0.1 ± 0.0
Low cooling rate (0.3K/s)					
0V	0.1 ± 0.1	0.0 ± 0.0	-	0.0 ± 0.0	0.0 ± 0.0
600ppm V	0.7 ± 0.3	0.4 ± 0.2	46.6 ± 11.8	0.1 ± 0.0	0.0 ± 0.0
0.2wt% V	2.1 ± 0.6	1.4 ± 0.4	16.2 ± 4.6	0.1 ± 0.1	0.0 ± 0.0
0.2wt% V + GR	3.0 ± 1.0	2.0 ± 0.7	12.2 ± 7.0	0.1 ± 0.1	0.0 ± 0.0

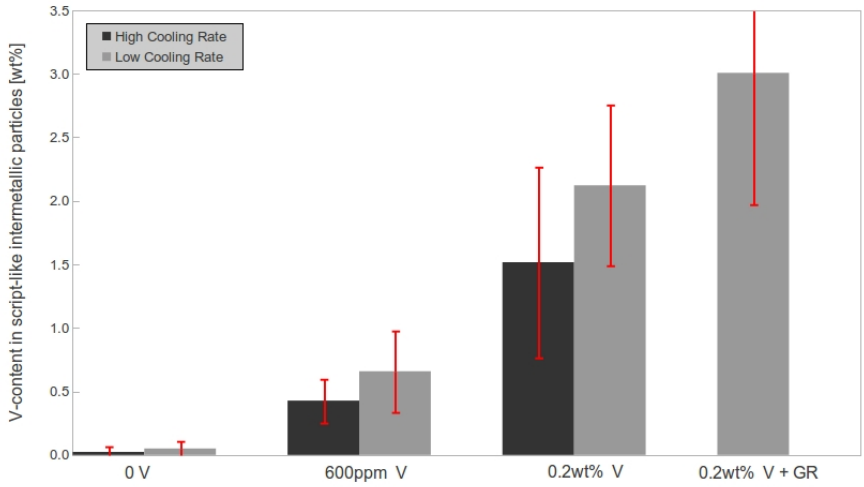

Figure 4.15: Average V-content in Chinese script-like particles [wt%] shown as a function of the nominal V-content in the alloy as given in Table 4.5. Dark grey markers indicate high cooling rate (0.9 K/s) and light grey indicate low cooling rate (0.3K/s). GR refers to grain refiner (TiB_2). The average V-content in the particles increases with increasing V-content in the alloys, and the average V-content is higher for the low cooling rate.

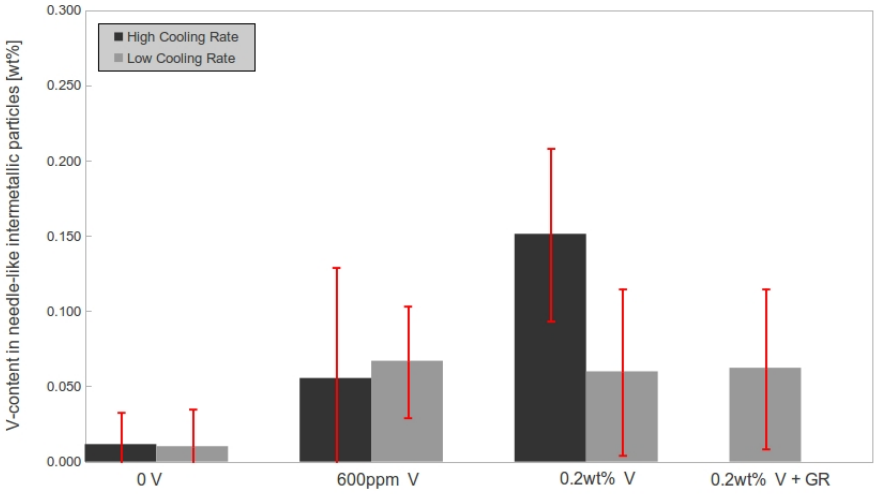

Figure 4.16: Average V-content in needle-like particles [wt%] shown as a function of the nominal V-content in the alloy. Dark grey markers indicate high cooling rate (0.9 K/s) and light grey indicate low cooling rate (0.3K/s). These values are found in Table 4.5, however in the table they are rounded to one decimal. GR refers to grain refiner (TiB_2).

4.5.2 Element ratios in Fe-rich intermetallic particles

The elemental ratios of Al/Si and Fe/Si were calculated based on at%. The average ratios for Chinese script-like Fe-rich intermetallic particles are given in Table 4.6. The Fe/Si-ratios are relatively even and indicate a value of 2. The Al/Si-ratio varies over a large span from 6.3 to 9.5. According to the probable phase α-Al_8Fe_2Si, the Fe/Si-ratio should be 2.

The average ratios for needle-like Fe-rich intermetallic particles are given in Table 4.7. The average Fe/Si-ratios are between 0.6 and 1. According to the probable phase β-Al_5FeSi, the Fe/Si-ratio should be 1.

Table 4.6: The average Fe/Si- and Al/Si-ratios for the Chinese script-like Fe-rich intermetallic particles based on at%. GR refers to grain refiner (TiB_2). The Fe/Si-ratio indicates a value close to 2, while the Al/Si-ratios covers a large span from 6.3 to 9.5 with relatively large standard deviations.

	Fe/Si-ratio		Al/Si-ratio	
	10.9 K/s [wt%]	0.3 K/s [wt%]	0.9 K/s [wt%]	0.3 K/s [wt%]
0 V	1.9 ± 0.5	2.2 ± 0.1	6.6 ± 1.5	6.3 ± 0.8
600ppm V	2.2 ± 0.3	2.1 ± 0.3	9.5 ± 3.3	6.6 ± 1.1
0.2wt% V	2.2 ± 0.4	1.9 ± 0.2	8.1 ± 2.0	6.3 ± 0.9
0.2wt% V + GR	-	2.0 ± 0.1	-	6.2 ± 1.0

Table 4.7: The Fe/Si- and Al/Si-ratios for the needle-like Fe-rich intermetallic particles based on at%. GR refers to grain refiner (TiB_2). The Fe/Si-ratios indicate a value of 1 or lower, while the Al/Si-ratios vary between 2.5 and 3.5 with significant standard deviations.

	Fe/Si-ratio		Al/Si-ratio	
	0.9 K/s [wt%]	0.3K/s [wt%]	0.9 K/s [wt%]	0.3K/s [wt%]
0 V	0.7 ± 0.1	1.0 ± 0.1	3.1 ± 1.2	3.0 ± 0.2
600ppm V	0.6 ± 0.1	1.0 ± 0.1	2.5 ± 0.7	3.1 ± 0.2
0.2wt% V	1.0 ± 0.1	0.9 ± 0.1	3.2 ± 1.3	2.9 ± 0.4
0.2wt% V + GR	-	0.9 ± 0.1	-	3.5 ± 1.3

4.6 Identification of Fe-rich intermetallic particles

The identification was conducted on the low cooling rate alloys, as little needle-like particles were found in the high cooling rate alloys. Also, the Chinese script-like particles were larger for the low cooling rate and therefore easier to perform EBSD and EDS on.

4.6.1 Chinese script-like particles

Below follows secondary electron (SE) micrographs, EDS- and EBSD-results for two Chinese script-like intermetallics. EBSD indexing was also attempted in a 0.2wt% V alloy. All the script-like particles analysed were V-rich. The EBSD indexing failed for hexagonal Al_8Fe_2Si in all cases. An example of one of these particles is given in Appendix I.

In Figure 4.17 a script-like Fe-rich intermetallic particle in the 0.3wt% Fe and no V alloy is presented with indications of points where EDS analysis was done. The corresponding EDS results are given in Table 4.8 and an EDS spectrum is found in Figure 4.19. The atomic Fe/Si and Al/Si ratios suggests a phase close to Al_6Fe_2Si. EDS maps of Al (a), Si (b), Fe (c) and V (d) is shown in Figure 4.18. The particle is seen to be Fe-rich and not containing V as the alloy is not added V.

Finally an unindexed (a) and indexed (b) EBSD pattern is given in Figure 4.20. The indexing is done according to the hexagonal Al_8Fe_2Si-phase found in the OIM software database [41]. The indexing gave a confidence index (CI) of 0.400.

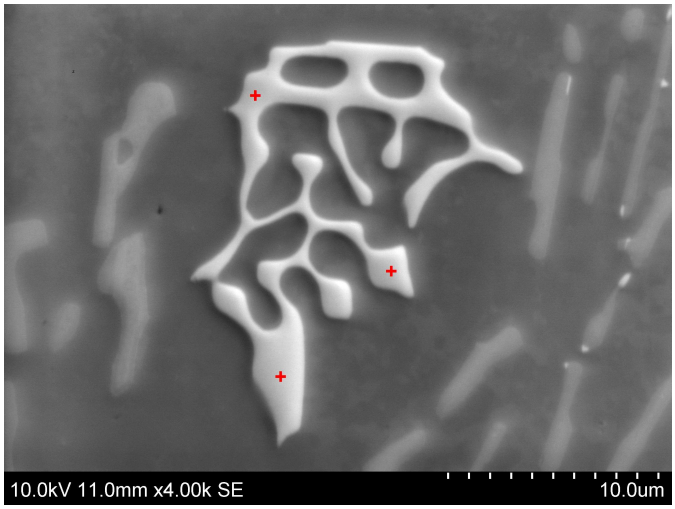

Figure 4.17: SE micrograph of a Chinese script-like intermetallic particle in the low cooling rate, 0.3wt% Fe and 0 V. The red crosses indicate points were EDS analysis was conducted. The EDS results are shown in Table 4.8. The light grey particles seen around the particle is eutectic Si.

Table 4.8: The quantification results for the EDS conducted on the three points shown in Figure 4.17. One of the representative EDS-spectra obtained and used for quantification is shown in Figure 4.19. The alloy has not been added V so the EDS shows no V accumulation in the particle.

	Al [at%]	Si [at%]	Fe [at%]	V [at%]	Fe/Si	Al/Si
Analysis 1	67.1	11.1	21.8	0.0	2.0	6.0
Analysis 2	66.8	10.8	22.3	0.0	2.1	6.2
Analysis 3	66.4	10.7	22.9	0.0	2.1	6.2
Average	66.8 ±0.3	10.9±0.2	22.3±0.6	0.0	2.1±0.1	6.1±0.1

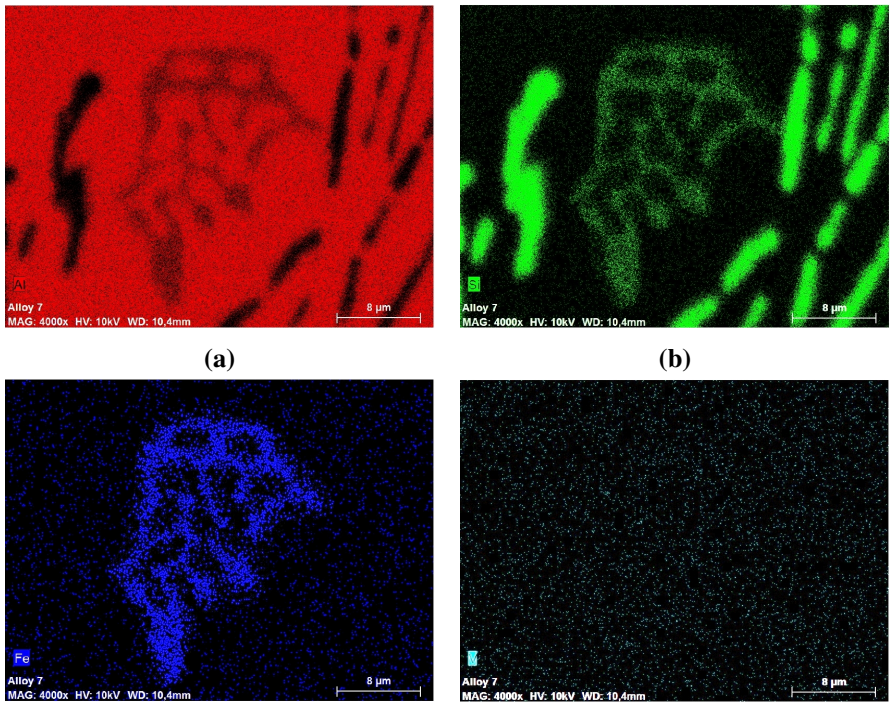

Figure 4.18: EDS maps of the particle shown in Figure 4.17; (a) Al, (b) Si, (c) Fe and (d) V. The particle contains Al, Si and Fe but no V (due to no nominal V additions). Silicon particles are observed around the particle (b).

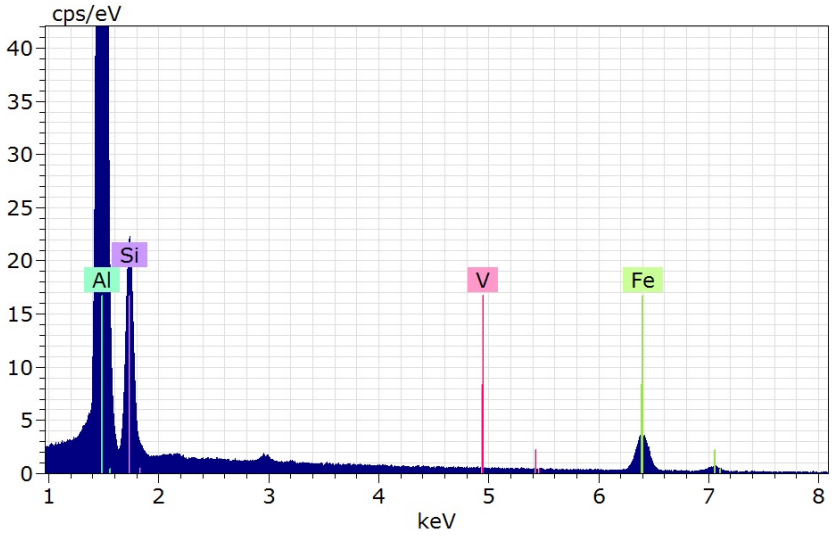

Figure 4.19: A representative EDS-spectrum of one of the points on the intermetallic particle shown in Figure 4.17. The spectrum shows a peak for Fe and no peak for V (due to no nominal V additions). The small peak at about 3keV is a shadow peak of the Al-peak.

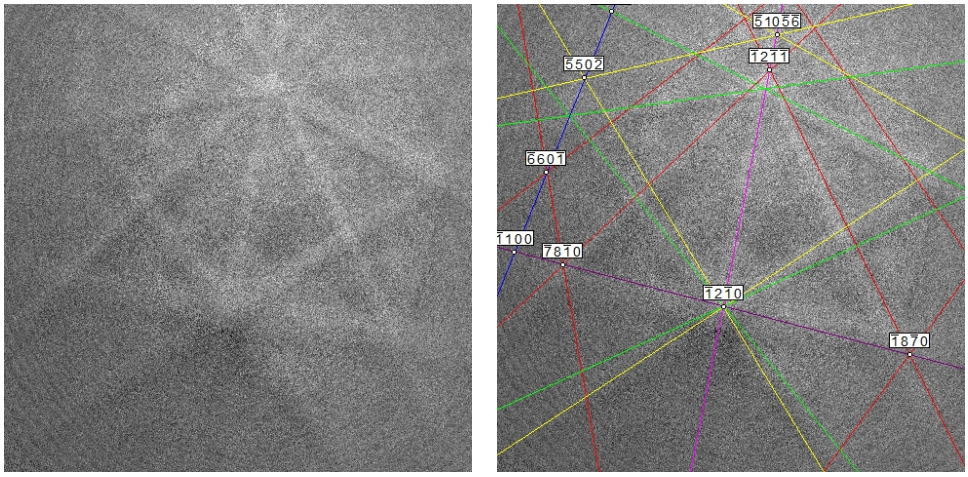

(a) **(b)**

.

Figure 4.20: (a) The EBSD pattern obtained from the particle in Figure 4.17. (b) The indexed EBSD pattern is indexed according to the hexagonal Al_8Fe_2Si. The indexing gave a confidence index of 0.400. The reflectors seen are $3\ 0\ \bar{3}\ 0,\ 2\ 3\ \bar{5}\ 6,\ 2\ 0\ \bar{2}\ 5,\ 3\ 0\ \bar{3}\ 10,\ 3\ 3\ \bar{6}\ 0$ and $0\ 0\ 0\ 12$

Corresponding results follow for the 0.3wt% Fe and 600ppm V alloy. In Figure 4.21 a micrograph of a Chinese script-like particle is presented with indications of where point EDS analysis was done. The EDS results of the points are given in Table 4.9 and a representative EDS spectrum is shown in Figure 4.23. The atomic Al/Si and Fe/Si ratios indicate a composition of roughly $Al_{6.5}Fe_2Si$. Vanadium is also measured in the phase. EDS maps for Al (a), Si (b), Fe (c) and V (d) follows in Figure 4.22 showing the presence of Al, Si and Fe in the phase. The V map (d) shows no special features.

Finally an unindexed (a) and indexed (b) EBSD pattern is shown i Figure 4.24. The indexing is done according to the hexagonal Al_8Fe_2Si-phase found in the OIM software database [41]. The indexing gave a confidence index (CI) of 0.679.

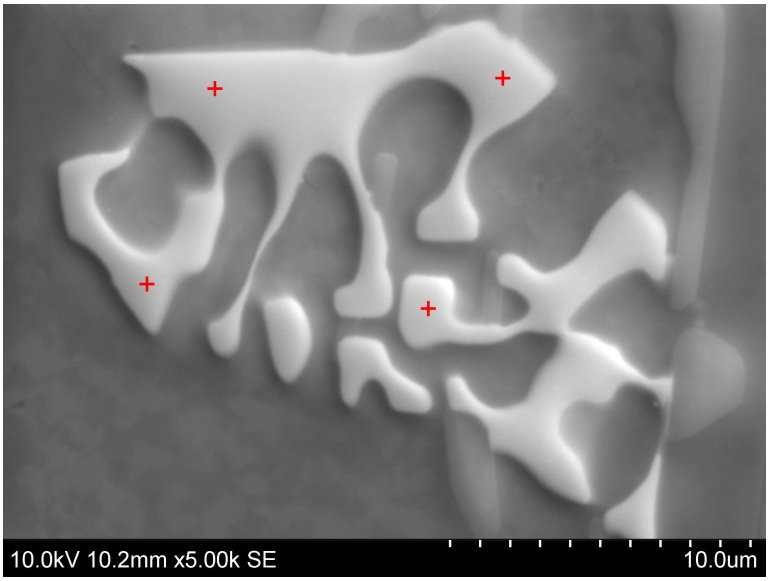

Figure 4.21: SE micrograph of a Chinese script-like intermetallic particle in the low coling rate, 0.3wt% Fe and 600ppm V. The red crosses indicate points were EDS analysis was conducted. The EDS results are shown in Table 4.9. The light grey particles seen around the particle is eutectic Si.

Table 4.9: The quantification results for the EDS conducted on the four points shown in Figure 4.21. One of the representative EDS-spectra obtained and used for quantification is shown in Figure 4.23. V is measured in the particle.

	Al [at%]	Si [at%]	Fe [at%]	V [at%]	Fe/Si	Al/Si
Analysis 1	66.4	10.6	22.7	0.3	2.1	6.3
Analysis 2	66.6	11.3	21.7	0.3	1.9	5.9
Analysis 3	71.6	10.0	18.0	0.4	1.8	7.2
Analysis 4	71.0	10.2	17.4	0.5	1.7	7.0
Average	68.9±2.8	10.5±0.6	20.0±2.6	0.4±0.1	1.9±0.2	6.6±0.6

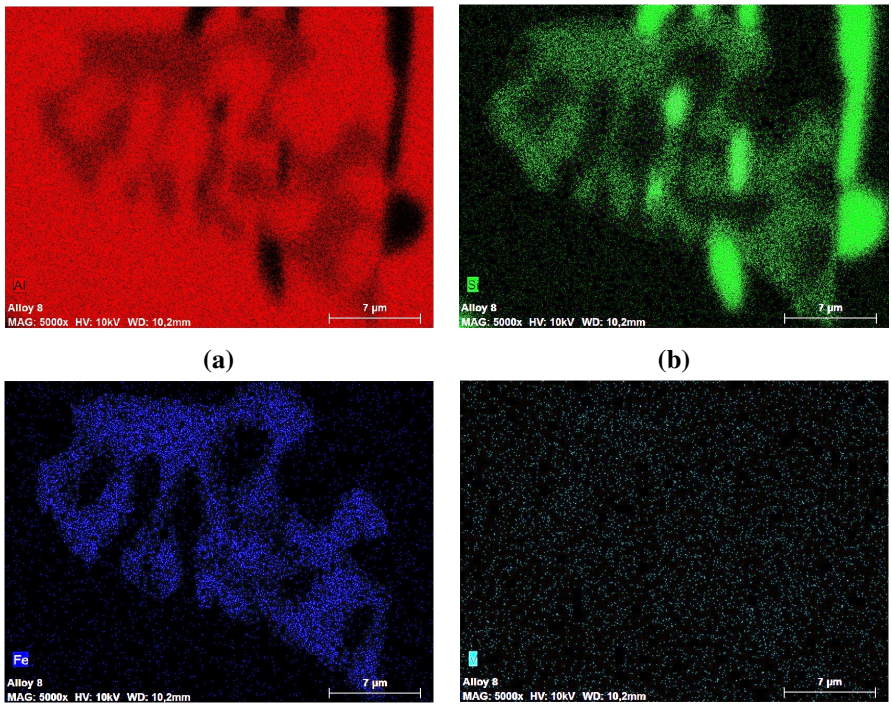

Figure 4.22: EDS maps of the particle shown in Figure 4.21, (a) Al, (b) Si, (c) Fe and (d) V. The particle clearly contains Al, Si and Fe, but the V map shows no conclusive features. Silicon particles are observed around the particles (b).

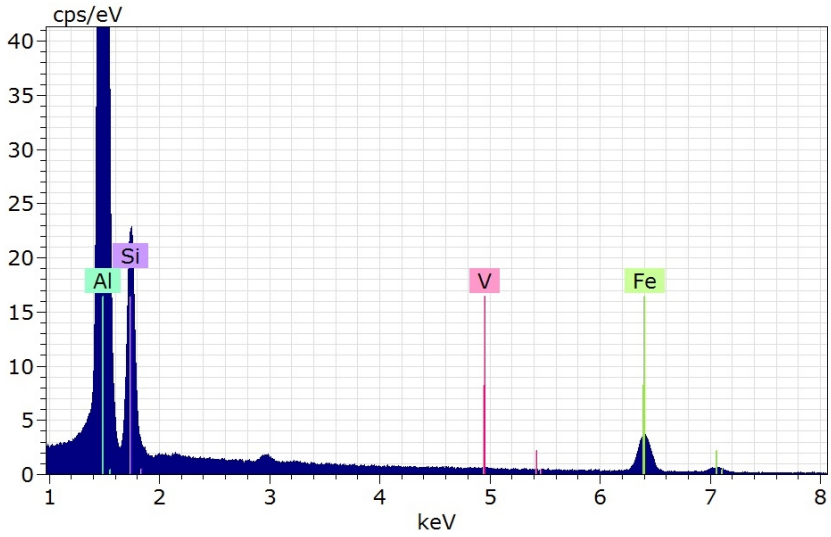

Figure 4.23: A representative EDS-spectrum of one of the points on the intermetallic particle shown in Figure 4.21. The spectrum shows a peak for Fe, but no definite peak for V can be distinguished. The peak at around 3keV is a shadow peak of the Al-peak.

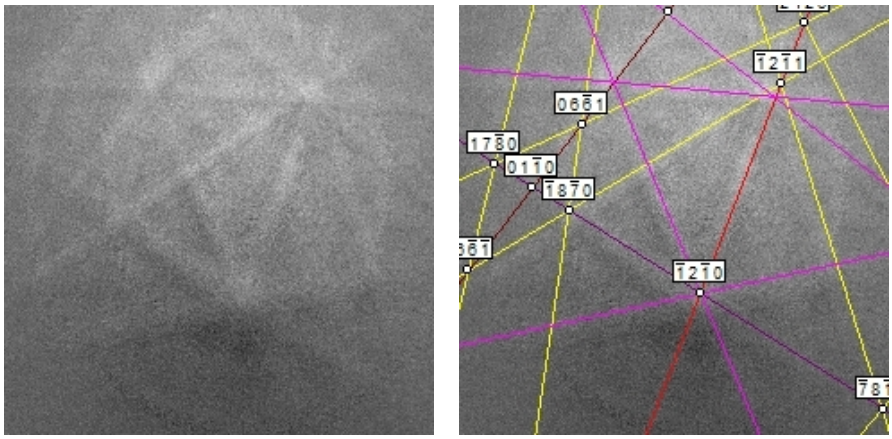

(a) **(b)**

Figure 4.24: (a) EBSD pattern obtained from the particle in Figure 4.21. (b) The indexed EBSD pattern is indexed according to the hexagonal Al_8Fe_2Si. The indexing gave a confidence index of 0.679. The reflectors seen are $3\,3\,\bar{6}\,0$, $3\,0\,\bar{3}\,0$, $0\,0\,0\,12$, $2\,3\,\bar{5}\,6$ and $3\,0\,\bar{3}\,10$

4.6.2 Needle-like particles

Micrograph, EDS- and EBSD-results for two intermetallic needle-like Fe-rich intermetallic particles are presented. In Figure 4.25 a needle-like particle in the 0.3wt% Fe and no V alloy is shown with indications of points where EDS analysis was done. The corresponding EDS results are given in Table 4.10 with a representative EDS spectrum in Figure 4.23. The atomic Fe/Si and Al/Si ratios suggests a phase close to Al_3FeSi. EDS maps of Al (a), Si (b), Fe (c) and V (d) is shown in Figure 4.26. No V is measured in the particle.

Finally, an unindexed (a) and indexed (b) EBSD pattern is shown i Figure 4.28. The indexing is done according to the monoclinic $Al_{4.5}FeSi$-phase found in the OIM software database [41]. The indexing gave a confidence index (CI) of 0.429.

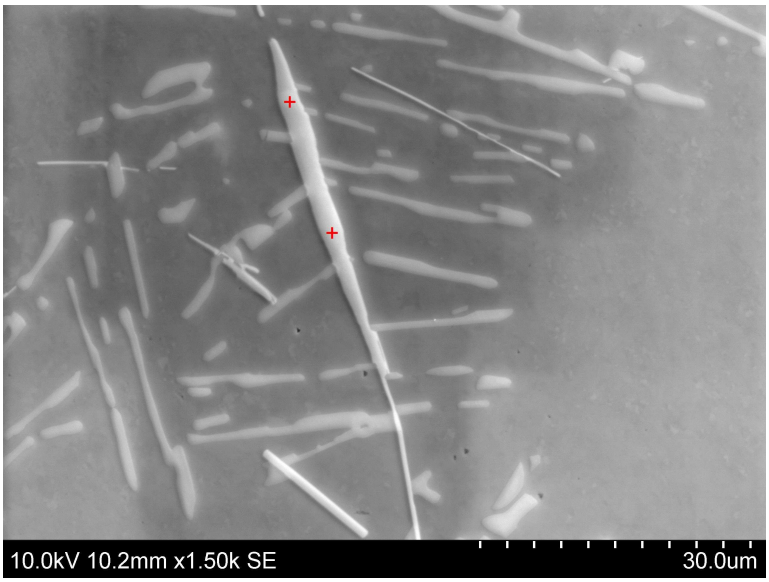

Figure 4.25: SE micrograph of a needle-like intermetallic particle in the low cooling rate, 0.3wt% Fe and 0 V alloy. The red crosses indicate points were EDS analysis was conducted, the results of which can be found in Table 4.10. The light grey particles seen around the particle is eutectic Si.

Table 4.10: The quantification results for the EDS conducted on the two points shown in Figure 4.25. One of the representative spectra used obtained and used for quantification is shown in Figure 4.27. No V is measured in the particle (no V was added the alloy).

	Al [at%]	Si [at%]	Fe [at%]	V [at%]	Fe/Si	Al/Si
Analysis 1	60.4	20.8	18.8	0.0	0.9	2.9
Analysis 2	59.8	20.1	20.8	0.0	1.0	3.0
Average	60.1±0.4	20.5±0.5	19.8±1.4	0.0	1.0±0.1	3.0±0.1

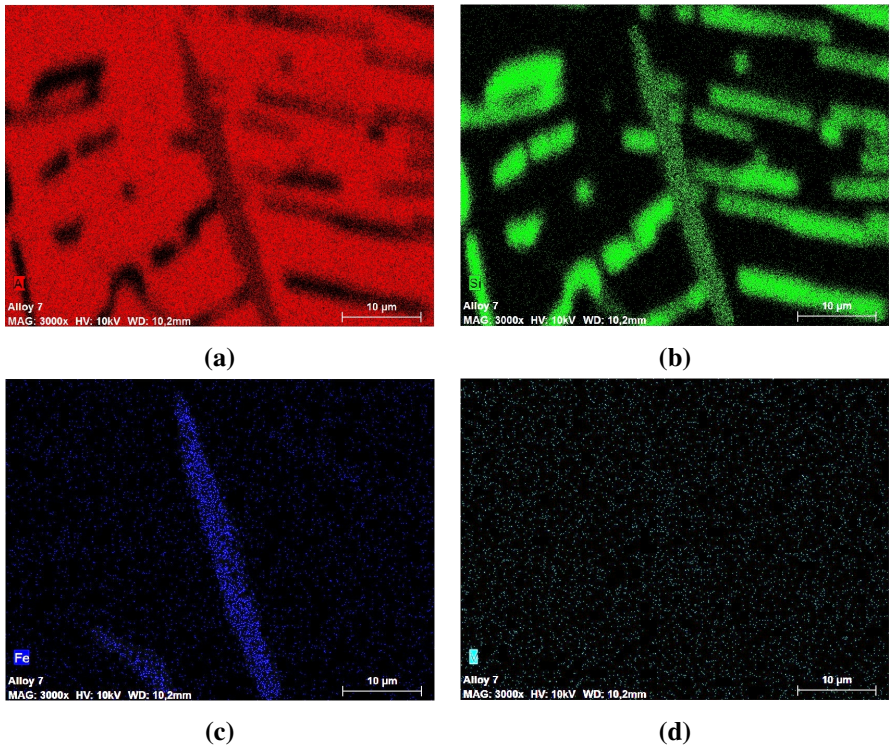

Figure 4.26: EDS maps of the particle shown in Figure 4.25; (a) Al, (b) Si, (c) Fe and (d) V. The particle clearly contains Al, Si and Fe. As expected no features are seen on the V map, due to no nominal additions of V in the alloy. Silicon is observed around the particle (b).

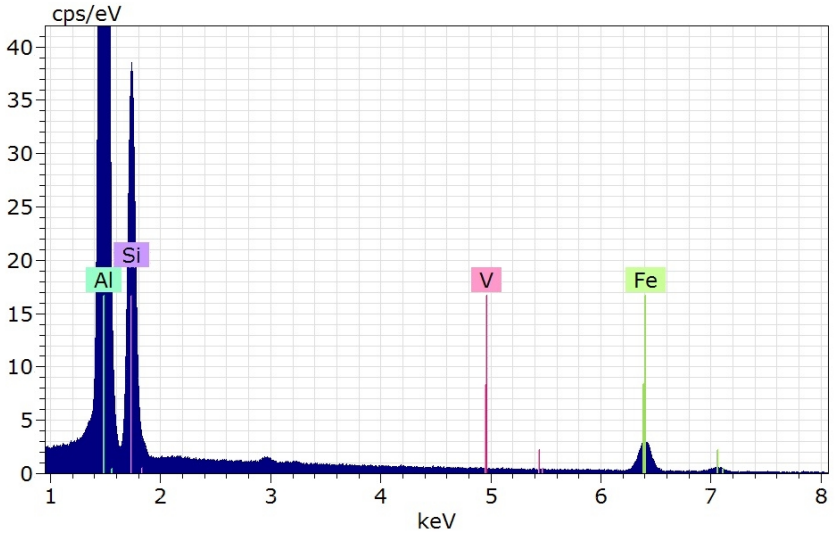

Figure 4.27: A representative EDS-spectrum of one of the points on the intermetallic particle shown in Figure 4.25. The spectrum shows a peak for Fe and as expected no peak for V due to no nominal V-additions in the alloy. The peak at around 3keV is a shadow peak of the Al-peak.

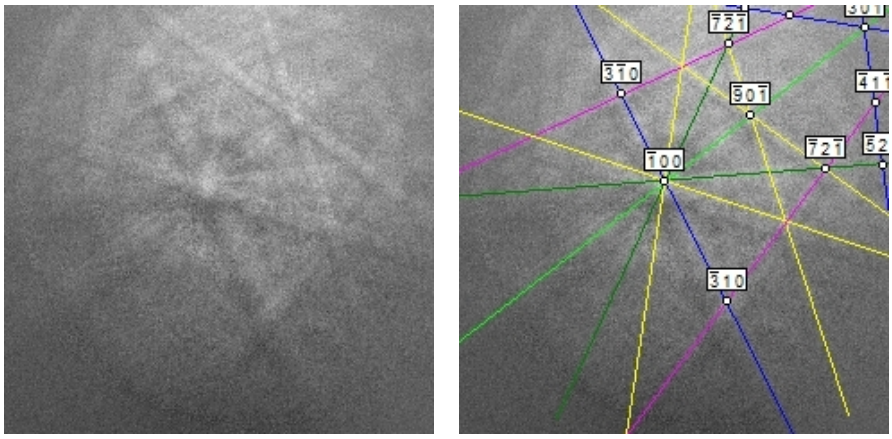

. **(a)** **(b)**

Figure 4.28: (a) EBSD pattern obtained from the particle in Figure 4.25. (b) The indexed EBSD pattern is indexed according to the monoclinic $Al_{4.5}FeSi$. The indexing gave a confidence index of 0.429. The reflectors seen are $0\,4\,8,\ 1\,1\,\bar{9},\ 3\,3\,\bar{9},\ 1\,3\,\bar{1},\ 0\,6\,0,\ 0\,2\,8$ and $0\,0\,4$

Corresponding results for the 0.3wt% Fe and 600ppm V alloy follows. In Figure 4.29 a micrograph of the needle-like particle is presented. The EDS results of the points are given in Table 4.11 and a representative EDS spectrum in displayed in Figure 4.31. The atomic Fe/Si and Al/Si ratios suggests a phase close to Al_3FeSi. EDS maps for Al (a), Si (b), Fe (c) and V (d) follows in Figure 4.30. No V is measured in the particle.

Finally an unindexed (a) and indexed (b) EBSD pattern is shown i Figure 4.32. The indexing is done according to the monoclinic $Al_{4.5}FeSi$-phase found in the OIM software database [41]. The indexing gave a confidence index (CI) of 0.486.

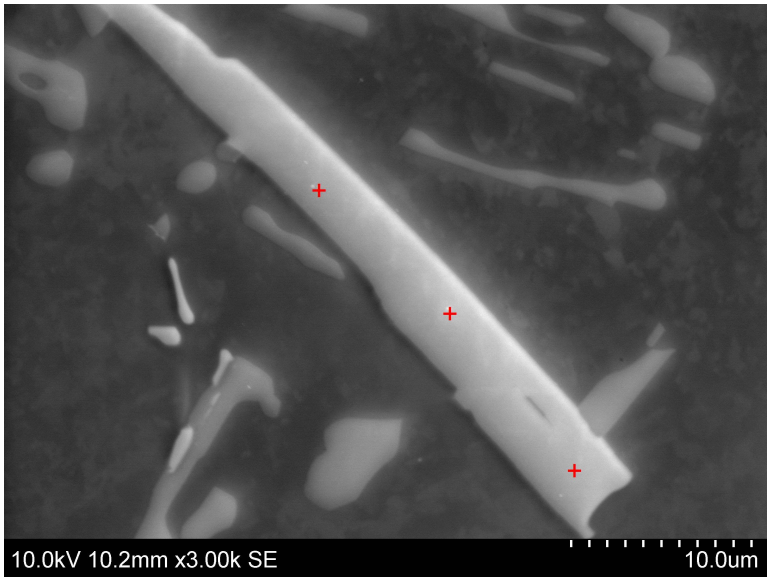

Figure 4.29: SE micrograph of a needle-like intermetallic particle in the low cooling rate, 0.3wt% Fe and 600ppm V alloy. The red crosses indicate points were EDS analysis was conducted, the results of which can be found in Table 4.11. The light grey particles are eutectic Si.

Table 4.11: The quantification results for the EDS conducted on the three points shown in Figure 4.29. One of the representative spectra used obtained and used for quantification is shown in Figure 4.31. No V is measured in the particle.

	Al [at%]	Si [at%]	Fe [at%]	V [at%]	Fe/Si	Al/Si
Analysis 1	59.3	20.0	20.7	0.0	1.0	3.0
Analysis 2	61.4	19.1	19.5	0.0	1.0	3.2
Analysis 3	62.1	19.8	18.1	0.0	0.9	3.1
Average	60.9±1.5	19.6±0.5	19.4±1.3	0.0	1.0±0.1	3.1±0.1

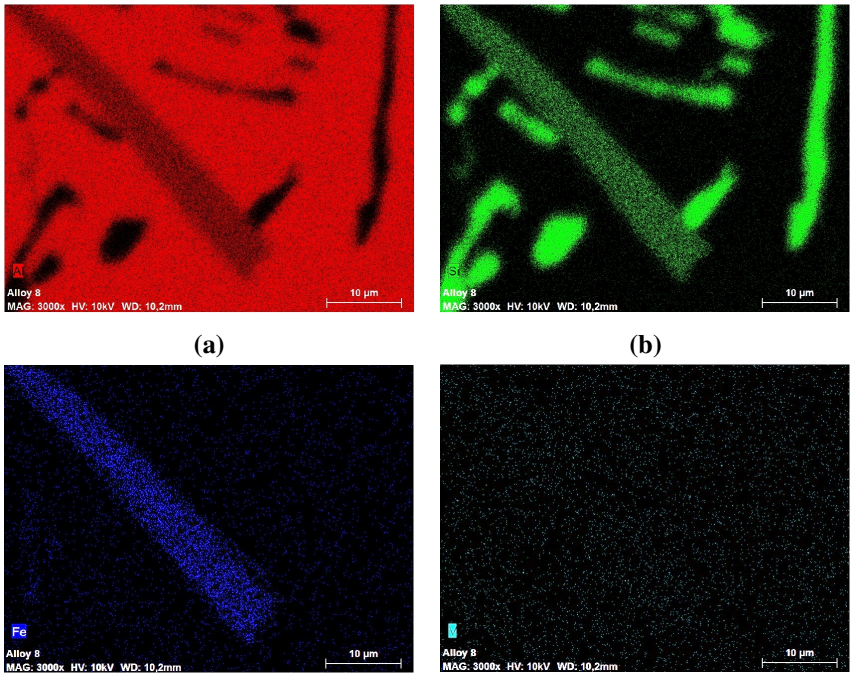

Figure 4.30: EDS maps of the particle shown in Figure 4.29; (a) Al, (b) Si, (c) Fe and (d) V. The particle clearly contains Al, Si and Fe and no features are seen in the V map. Si is observed around the particle (b).

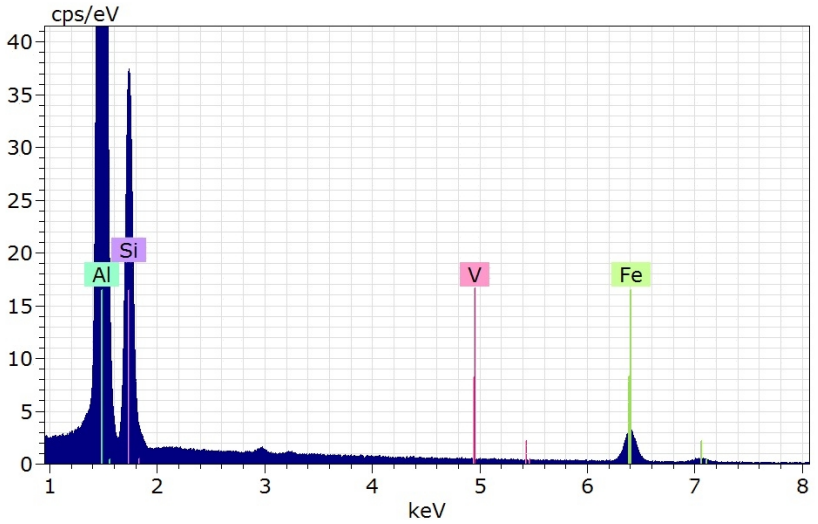

Figure 4.31: A representative EDS-spectrum of one of the points on the intermetallic particle shown in Figure 4.29. A peak for Fe is seen but no peak for V is observed. The peak at around 3keV is a shadow peak of the Al-peak.

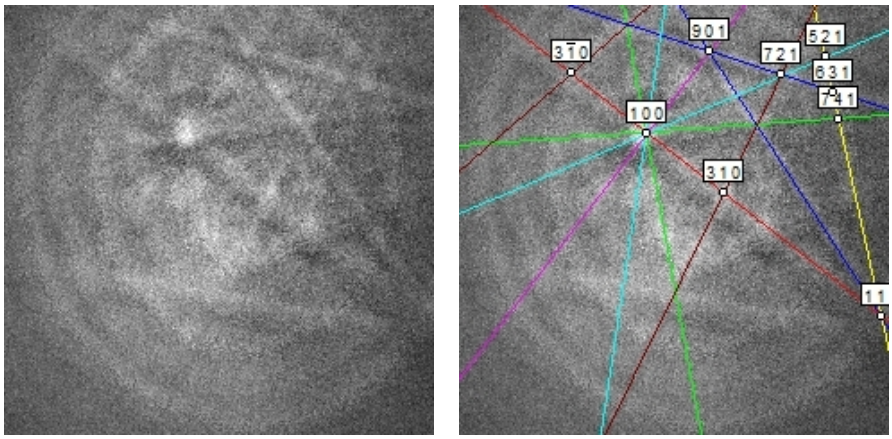

(a) **(b)**

Figure 4.32: (a) EBSD pattern obtained from the particle in Figure 4.29. (b) The indexed EBSD pattern is indexed according to the monoclinic $Al_{4.5}FeSi$. The indexing gave a confidence index of 0.486. The reflectors seen are $1\,3\,\bar{1}$, $0\,6\,0$, $1\,1\,\bar{9}$, $0\,2\,8$, $3\,3\,\bar{9}$, $0\,0\,4$ and $0\,4\,8$

4.7 Macroetched samples

Samples of both the high and low cooling rate alloys were etched in a solution of methanol and iodine. This solution removed the aluminium, thus making it possible to view the 3D appearance of the intermetallic particles and eutectic silicon.

Micrographs of a branched particle and a more blocky Fe-rich intermetallic particle is shown in Figure 4.33. In a cross section these particles could appear as Chinese script-like. The corresponding EDS-maps are shown in Figure 4.34 for Al (a), Si (b), Fe (c) and V (d). Both particles are clearly Fe-rich and seem to contain V.

A plate shaped particle is shown in Figure 4.35. In a cross section this particle would obtain a needle-like shape. Both particles were found in the high cooling rate 0.3wt% Fe and 0.2wt% V alloys. The corresponding EDS-maps are shown in Figure 4.36 for Al (a), Si (b), Fe (c) and V (d). The plate is clearly Fe-rich and no features are seen on the V map.

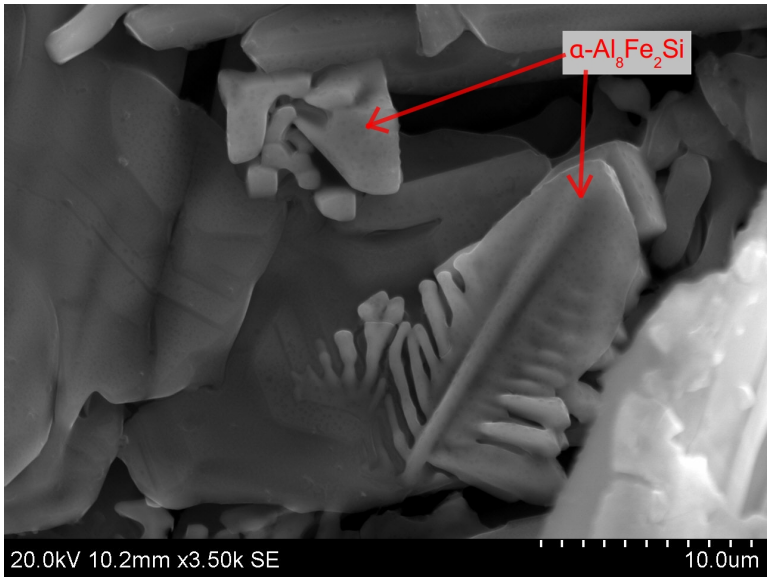

Figure 4.33: Micrograph of two Fe-rich intermetallic particles in a low cooling rate, 0.3wt% Fe and 0.2wt% V etched alloy. The particle down to the right has a branched appearance in 3D and the other appear more blocky. Both would probably appear as Chinese script-like in 2D if a cross section would have been made.

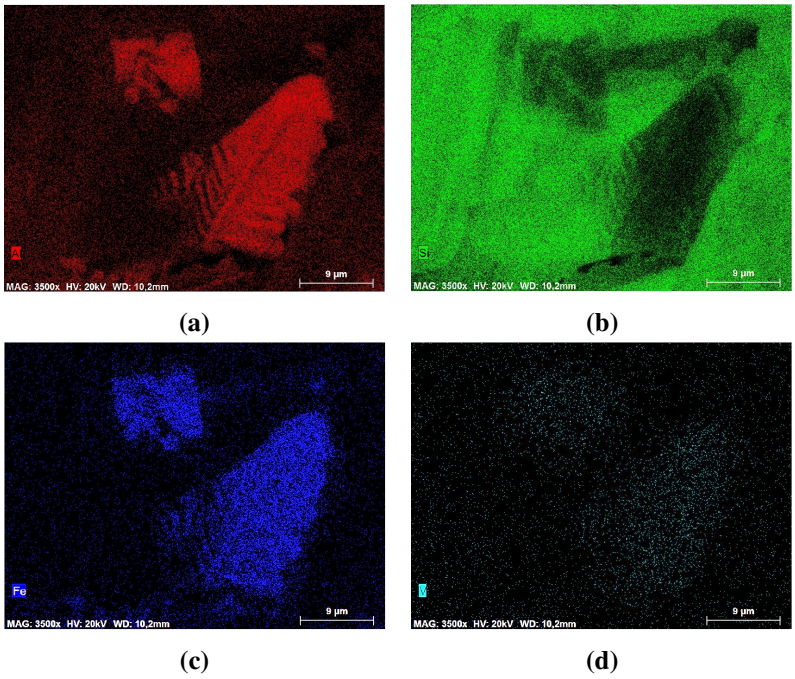

Figure 4.34: EDS maps of the area shown in Figure 4.33; (a) Al, (b) Si, (c) Fe and (d) V. The particle is clearly Fe-rich (c) and seems to contain V (d). The surrounding phases are mainly Si.

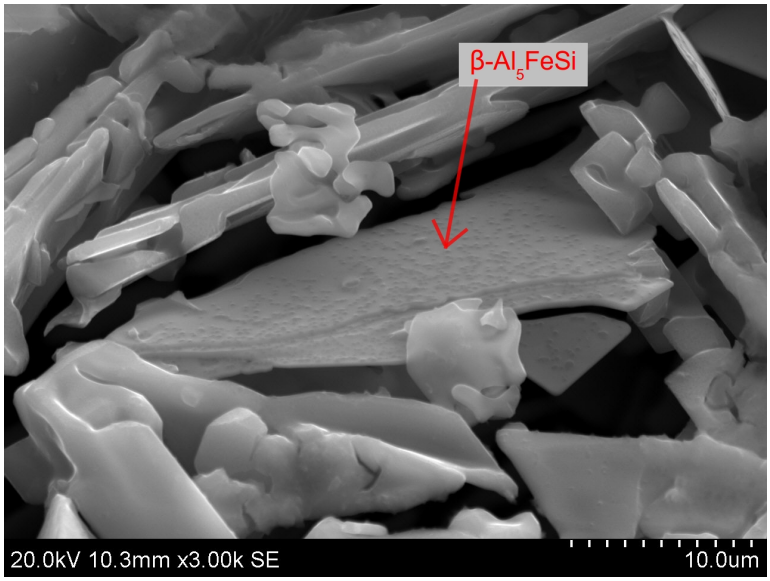

Figure 4.35: Micrograph of a plate-shaped particle in a low cooling rate 0.3wt% Fe and 0.2wt% V etched alloy. The surrounding platelets are silicon which has a more rounded appearance compared to the sharp edged β-platelet.

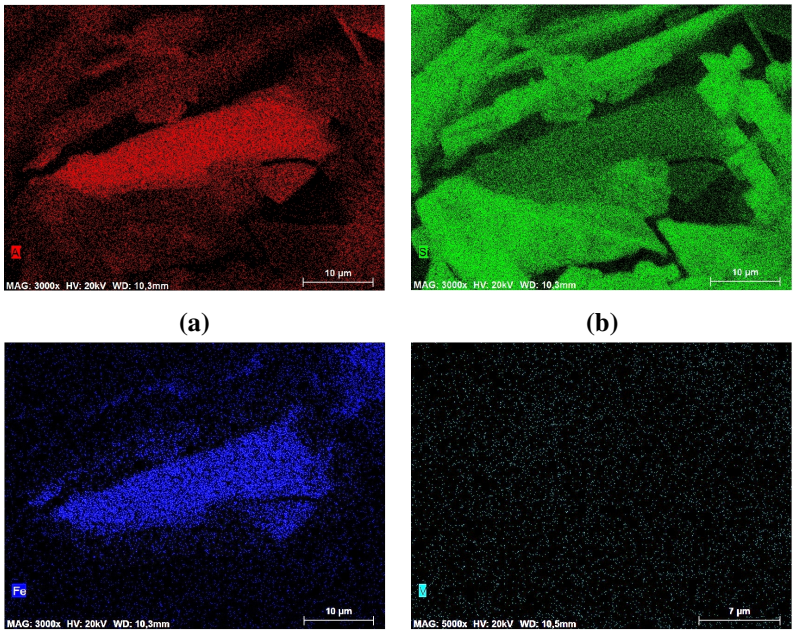

Figure 4.36: EDS maps of the area shown in Figure 4.35; (a) Al, (b) Si, (c) Fe and (d) V. The particle is clearly Fe-rich (c) and no V is observed (d). The surrounding phases are mainly Si.

Chapter 5

Discussion

5.1 Intermetallic particle identification

For both Chinese script-like intermetallic particles, seen in Figures 4.17 (0 V alloy) and 4.21 (600ppm V alloy), Tables 4.8 and 4.9 give average atomic Fe/Si-ratios of 2.1 and 1.9, respectively. The Fe/Si-ratios are in agreement with the stoichiometry of the α-Al_8Fe_2Si phase. A separate EDS-analysis was done on both script- and needle-like particles in all the alloys and the elemental ratio results for scripts are given in Table 4.6. Here the average atomic Fe/Si-ratios are around 2 and in agreement with the α-phase as well.

The needle-like particles were analysed in the same manner as the Chinese script-like particles. A needle-like particle is shown in Figure 4.25 for the 0 V alloy and for the 600ppm V alloy in Figure 4.29. The average atomic Fe/Si-ratios in Tables 4.10 and 4.11 are 1.0. According to the β-phase, the stoichiometry should be Al_5FeSi or $Al_{4.5}FeSi$. The average atomic Fe/Si-ratio is in good agreement with this, as is the EDS analysis of needles in all the alloys (see Table 4.7), with an average atomic Fe/Si-ratio also close to 1.

For several Chinese script-like particles EBSD indexing according to hexagonal α-Al_8Fe_2Si was done. The EBSD-patterns in Figures 4.20 (0 V alloy) and 4.24 (600ppm V alloy) gave confidence indexes (CIs) of 0.400 and 0.679, respectively. Since it has been shown that a CI$>$0.1 yields the correct solution 95% of the time [54], the indexing of the script-like particles seem to confirm that the particles are hexagonal α-Al_8Fe_2Si. The particles described as script-like will therefore be assumed to be hexagonal α from here on.

The EBSD indexing for the needle-like particles was done according to monoclinic $Al_{4.5}FeSi$, the results presented in Figures 4.28 (0 V) and 4.32 (600ppm V). The CIs were 0.429 and 0.486, respectively. These are very good CIs which seem to confirm monoclinic β-$Al_{4.5}FeSi$. The particles described as needle-like will therefore be assumed to be monoclinic β from here on.

5.2 Vanadium in particles

The EDS analysis in Table 4.9 shows V in a Chinese script-like particle for the 600ppm V alloy. From the EDS analysis done on script-like particles in all the alloys, Table 4.5 and Figure 4.15, the V accumulation in script-like particles is found to increase upon increasing V-content in the alloy. This suggests that V can be accumulated in the script-like particles [26].

If there is a change in structure of the α-particles upon V-additions, as is the case for Mn, was not specifically addressed in this investigation. However, attempts to index EBSD patterns according to the hexagonal α obtained from vanadium enriched script-like particles in the 0.2wt% V alloy was unsuccessful. An example showing such a V enriched script-like particle is shown in Appendix I. EBSD-patterns for cubic α was not found in the indexing software's database and indexing according to this was therefore not attempted. The possibility that V stabilizes the α-phase and creates a cubic structure, as proposed by several authors (e.g. Munson [25] and Skinner et al. [26]) and shown by Wang et al. [28], could therefore seem plausible. However, the average V-content in the script-like particles (see Table 4.15) peaked at 3.0wt% (2.0 at%) which gives a very high atomic Fe/V ratio (the lowest around 12) indicating that only a few Fe-atoms were substituted. For Mn an example of corresponding values (Table 2.1) shows Mn-contents 8.36 and 8.49wt%, giving atomic Fe/Mn ratios of 2.23 and 2.18 in the α-particles. Further investigations either by EBSD or TEM could be conducted to investigate if there is a change in the crystal structure by the replacement of Fe by V, as it is for Mn.

The V-content in the α-particles was higher for the low cooling rate, as seen graphically in Figure 4.15. This is probably because the vanadium is given more time to segregate in the liquid when the cooling rate is lower so that more can be captured within an α-particle. There seems to be a minor increase in V-accumulation in the script-like particles in the grain refined alloy, however the standard deviations are large. The increase could be a result of the decrease in amount of α-particles (as will be discussed later) when grain refiner is present. Fewer α-particles would then be competing for the vanadium in the near vicinity of the particle.

The EDS analysis show some V measured in the β-particles, cf. Table 4.5. From this and the graphical representation in Figure 4.16, the V-contents are very low with relatively large standard deviations. The maximum V-concentration is found to be just below 0.2wt%. According to a previous study reproduced in Table 2.2 [29], 0.2wt% V was measured in particles with β resembling stoichiometry. The β-particles may therefore be able to dissolve small amounts of V.

5.3 α and β quantification

Based on the phase diagrams in Figures 2.1 and 2.2 the equilibrium solidification path can be estimated for Mn- and V-free alloys. The solidification paths for the alloy compositions at hand, 7wt% Si and 0.1 and 0.3wt% Fe, have been drawn in on Figure 2.2. Both the 0.1 and 0.3wt% Fe composition passes through aluminium dendrites, eutectic Al + Si and finally the eutectic E_1.

Upon solidification solute redistribution occurs and the solidification path alters as for the 0.8wt% Fe example shown in Figure 2.3. From this diagram the Fe_{crit} shows that pre-eutectic β would form in a 7wt% Fe alloy if the Fe-content is larger than approximately 0.4wt% Fe. For the 0.3wt% Fe alloy the path would therefore proceed through aluminium dendrites, eutectic Al + Si and finally the eutectic E_1. Since the alloy with high Fe-content reaches the main eutectic faster, more β would be expected to be formed. No α should form at these equilibrium conditions. According to the Alstruc [59] simulation, only β was predicted to form in alloys of both Fe-contents and both cooling rates. More β (higher volume%) is also predicted for higher Fe-content, in accordance with the solidification paths.

In the V-free alloys α was formed. For the high cooling rate alloys, the low Fe-content (0.1wt%) caused the α formed to have only a small Chinese script-like morphology (cf. Figure 4.1). For the high Fe-content (0.3wt%) almost all the Fe-rich intermetallic particles were script-like (cf. Figure 4.2) and the average area fraction of script, relative needles and script, was found to be 94% (Table 4.4). β has been found to be suppressed at high cooling rates [8]. The explanation is a decreased nucleation temperature of the β-phase down to the eutectic Si temperature, causing the phase mainly to form simultaneously and/or after the eutectic Si. The liquid depleted in Si would then favour the phase containing the least Si, thus favouring α-Al_8Fe_2Si (1 Si pr. 11 atoms) over β-Al_5FeSi (1 Si pr. 7 atoms) [8, 9]. This could account for the very amount of needle-like particles in the 0.9 K/s alloys and that α was formed in the 0.3K/s alloys.

If a fourth element such as Mn is introduced, changes in the phase diagram occur. Mn is known to stabilize the α-phase causing alterations to the phase diagrams as shown in Figures 2.5 and 2.6. The new Mn-containing α-phase would now be expected to form both in a binary reaction (Al + α) and a ternary eutectic reaction (Al + α + β), prior to the main eutectic Al + Si + β. Theoretical stabilization calculations, performed by Wang et al. [28], showed that V may stabilize the α-phase as well. The stabilization has also been confirmed in rapidly solidified Al-Fe-V-Si alloys [26, 27]. In light of this there could be a similarity between the effect of Mn and the effect of V on the Al-Fe-Si phase diagram.

5.3.1 Low cooling rate

The average relative fractions of α to α- and β-particles were reported for the low cooling rate alloys in Table 4.3. It is found to increase with increasing V-content in the alloy. It is also very clear that the average total area of Fe-rich intermetallic particles decrease with the V-content in the alloys from Figure 4.9.

From 0 V to 600ppm V the total average area decreases only a small amount and the average area of Chinese script-like particles increases on expense of the needle-like particles. Based on all the micrographs, examples shown in Figures 4.5 and 4.6, the main change is coarser script and shorter needles. This would be consistent with a similar change seen in Mn additions where a binary Al + α reaction appears, causing coarser α to form. Relatively coarse β is still present suggesting that the binary eutectic Al + β reaction still takes place, however the needles are shorter indicating that the reaction may have been suppressed somewhat. This would be consistent with a slight stabilization of α as shown for the phase diagram for low Mn addition in Figure 2.6a. The smaller α and β particles could stem from the main eutectic reaction Al + Si + β and/or the new ternary eutectic reaction Al + α + β.

From 600ppm to 0.2wt% V the average area of script-like particles doesn't change substantially, but the major decrease in average total area seems mainly due to a major decrease in average area of needles. Based on micrographs such as the one shown in Figure 4.7 the β is much finer than at the lower V-contents and both coarse and fine α is present. If further stabilization causes further change in the phase diagram, as for Mn, the coarse binary eutectic β would eventually disappear (see Figure 2.6 and 2.5). All β would form in ternary eutectic reactions, thus becoming fine needles. α would form in both binary and eutectic reactions causing both coarse and fine script to form. The major decrease in average total area of script and needles could therefore seem to be mainly due to a refinement of the β-needles due to suppression of the binary eutectic Al + β reaction.

The average total area of Chinese script-and needle-like particles decreases upon V-content. It was shown by Lu et al. [22] in a commercial alloy, that upon Mn additions the trend was opposite. It was explained as an effect of the substantial coarsening of the binary α forming, even though the β-needles become finer and fewer. However, the α-particles in this study was far less elaborate than the ones in that investigation. The refinement and decrease in amount of β-particles does therefore seem to be sufficient to have an effect on the average total area even though there is a coarsening of α.

For the low cooling rate a 0.2wt% Fe alloy was made with grain refiner (TiB_2). From Figure 4.9 it is found that the average total area of Fe-rich intermetallic particles is about the same as for the 0.2wt% Fe alloy without grain refiner. However, the area of script-like particles decreases. Based on Table 4.3 the average area fraction of script-like particles

(relative script and needles) is found to be 25%. Compared to the other low cooling rate alloys this value is about as low as for the V-free alloy. From Figure 4.8 the grain refined alloy is seen to have far more and coarser needles compared to the unrefined alloy. Since the needles become coarser it might suggest that binary eutectic β forms again. If the β area isn't displaced too much by the α area in the phase diagram, more like (a) than (b) in Figure 2.6, the binary eutectic Al + β reaction is still present. When no TiB_2 is present the nucleation temperature of β could be suppressed down to the eutectic reaction, a high undercooling (ΔT), so that no coarse binary eutectic β was formed. When grain refiner is added the nucleation temperature increases again, ΔT decreases, and binary β may form. Based on equation 2.3 this would cause a coarsening of the eutectic (larger λ). From this it seems that thes TiB_2-particle might aid the nucleation of needle-like particles as suggested other researchers [15] and cause the eutectic β to become coarser.

5.3.2 High cooling rate

All the 0.9 K/s alloys have less β than the 0.3K/s alloys, as seen from Tables 4.4 and 4.3. The average total area of intermetallic particles is very low for the 0 V alloy and increases from 0 to 600ppm V, then decreases from 600ppm to 0.2wt% Fe, cf. Figure 4.10.

If no Mn or V is present the amount of β should decrease as a result of the binary eutectic reaction Al + β proceeding faster compared to a lower cooling rate, cf. equation 2.2. In the high cooling rate alloy, there is almost no needles at all. There is also relatively little Chinese script and from the micrograph in Figure 4.2 the script is very small. It would therefore seem as if the binary eutectic Al + β reaction is suppressed and that the small α form as a result of α-particles being more favourable during the main eutectic reaction than β-particles.

By addition of 600ppm V there is an increase in the average total area of both types of intermetallic particles. From the micrograph in Figure 4.3 some script-like particles appear to have become coarser, however the change is minimal. This could be consistent with a binary Al + α reaction and a new ternary eutectic Al + α + β reaction which would yield more of both α and β. Since the binary eutectic β seems to be suppressed at this cooling rate, the increase in amount and coarseness of α is sufficient to increase the average area of Fe-rich intermetallic particles as proposed by Lu et al. [22].

By addition of 0.2wt% V there is a major change in the microstructure. In the micrograph there appears to be far less Fe-rich intermetallic particles and the script-like particles become coarser (Figure 4.4). The coarsened script could be explained as a result of stabilization of the α-area in the phase diagram (much like Figure 2.6a) causing the binary Al + α reaction to form coarser script. Based on the change in average total area of particles from 600ppm to 0.2wt% V, Figure 4.10, the average total area decreases as a

result of decrease only in area of script-like particles. Due to the increase in binary α, and suppression of binary eutectic β, the total area should continue to increase as from 0 to 600ppm V. It is possible that when binary α is formed, the concentration of Fe decreases and due to the cooling rate the remaining Fe may not segregate fast enough and less Fe-rich intermetallic particles would then be able to form in the following eutectic reaction(s).

There appear to be coarser needles in the 0.2wt% as well. However, when all the micrographs were examined the size of the needles were similar in both the 600ppm and the 0.2wt% Fe alloys.

5.4 Particle size distributions

The image analysis gave the area of every discrete particle. In the particle size distribution diagrams, Figures 4.11-4.14, the particle sizes $<5\mu m^2$ were omitted and the fractions only calculated on basis of particles $>5\mu m^2$. The obvious trend in all graphs are that the fraction of particles decreases with size class.

For the Chinese script-like particles, the vanadium content in the alloy does not seem to affect the sizes of the particles substantially and the fractions are relatively even. There does not seem to be any trend in particle sizes due to increasing V-content for the needle-like particles either. This is *not* in accordance with previously discussed results such as micrographs and the average total area which show differences in coarseness of particles.

For both the script- and needle-like particles the particles are larger in the low cooling rate alloy. This is seen as the low cooling rate alloys have a smaller fraction of particles in the 5-10μm^2 class, and a larger fraction of particles in the middle and higher size classes. This coarsening effect has been reported by others [11] and would be consistent with a lowering of the growth rate (lower growth velocity, V) causing more particles to form and the eutectic phases to become coarser (larger λ) according to equation 2.2.

The Chinese script-like particles in the grain refined alloy follow the size of the unrefined alloy quite well (Figure 4.11). For needle-like particles, Figure 4.13, the grain refined alloy clearly has larger particles as it peaks in the 10-15μm^2 size class compared to the 5-10μm^2 for the other alloys. It can also been seen from the micrographs in Figure 4.8 that the grain refined alloy has more and coarser needle-like particles. This supports the earlier findings of the increase in total average area of β-particles and the micrograph showing more and coarser needles in the grain refined alloy. This would follow from equation 2.3 as the undercooling (ΔT) is decreased due to the potent nuclei, thus increasing the lamellar spacing (λ).

The increase in coarseness of needles in the grain refined alloy was very obvious from the micrograph in Figure 4.8 and the area quantification in Table 4.3. Other changes in coarseness of needles and script were found from changes in V content, but not as extreme

as for the grain refiner addition. Since only the first was evident from the particle size distribution diagrams the accuracy of the software used for image analysis and its ability to pick up changes in coarseness is apparently not sensitive enough for the changes observed in this investigation.

The coarseness of Chinese script-like particles would manifest itself as more elaborate script. As seen in e.g. Figure 4.21 large script will appear as several smaller discrete particles when cut to a 2D section. An obviously more elaborate script-like particle will therefore be seen as several smaller ones by the software. Therefore, changes in script size and/or coarseness might not be measured by the software. For the needles the angle of the 2D surface and the platelet direction will also affect the area of the particle. If the plate is cut close to a corner or closer to the centre would affect the apparent length of the particle. A cross section 90° to the platelet would be more needle-like than one with a shallower angle. For these reasons several observations made earlier might not be seen from the distribution diagrams.

Chapter 6

Conclusions

The effect of V on Fe-rich intermetallic particles in a high purity Al-7wt% Si alloy was investigated. The work can be concluded as follows.

- Fe-rich Chinese script- and needle-like intermetallic particles were successfully identified as hexagonal α-Al_8Fe_2Si and monoclinic β-$Al_{4.5}FeSi$, respectively, by EBSD and atomic Fe/Si-ratios.
- The α-particles accumulated V and the amount increased with the V-content in the alloy. The Chinese script-like particles in the lower cooling rate alloys (0.3K/s) accumulated more V than the higher cooling rate alloys (0.9 K/s).
- The V-accumulation in β-particles were minor with a maximum of 0.2wt%.
- For the 0.3 K/s and 0.3wt% Fe alloys the average area fraction of α-particles to α+β-particles increased with increasing V-content in the alloys. The average total area of Fe-rich intermetallics decreased with increasing V-content.
- For the 0.9 K/s and 0.3wt% alloys the average relative area fraction of α-particles to α + β-particles was very high and decreased with increasing V-content in the alloys. The average total area of Fe-rich intermetallic particles increased from 0 to 600ppm V and decreased from 600ppm to 0.2wt% V.
- Addition of excess TiB_2 grain refiner to the 0.2wt% V alloy reduced the area fraction of α-particles to the level of the 0 V alloy. This was supported by micrographs and particle size distributions showing more and larger needles in this alloy.
- The changes in microstructure was explained as a stabilization of the α-phase similar to, but less effective than, the effect of Mn.

Chapter 7

Further Work

Structural analysis of the script-like particles in the 0.2wt% V alloy should be done. EBSD analysis according to the cubic α-phase is possible and it is also an alternative to prepare TEM samples and attempt to obtain diffraction patterns from the particles. It could also be possible to do extraction of Fe-rich intermetallic particles and do X-ray diffraction on them to determine the structure. If hexagonal α-particles were found in the V-containing samples, it could also be interesting to attempt heat treatment to see if that would alter the structure of more of the α-particles to cubic.

A more accurate EDS analysis could be done to obtain more accurate chemical composition measurements. EPMA is one possibility. If an etch exists that removes Si as well as Al and leaves the Fe-rich intermetallic particles, EDS in the SEM could be done directly on the particles without interference from the Al and Si matrix.

Bibliography

[1] N.A. Belov, A.A. Aksenov, and D.G. Eskin. *Iron in Aluminium Alloys: Impurity and Alloying Element*. Taylor & Francis Inc., London and New York, 2002.

[2] C.-L. Chen and R. C. Thomson. The combined use of EBSD and EDX analysis for the identification of complex intermetalllic phases in multicomponent Al-Si pistons. *Journal of Alloys and Compounds*, 490:293–300, 2010.

[3] Kazuhiro Nogita, Stuart D. McDonald, Katsuhiro Tsujimoto, Yasuda Kazuhiro, and Arne K. Dahle. Aluminium phosphide as a eutectic grain nucleus in hypoeutectic Al-Si alloys. *Journal of Electron Microscopy*, 53:361–369, 2004.

[4] J.A. Taylor. Iron-containing intermetallic phases in Al-Si based casting alloys. *Procedia Materials Science*, 1:19–33, 2012.

[5] John A. Taylor. *The role of iron in the formation of porosity in Al-Si-Cu alloy castings*. PhD thesis, The University of Queensland, Australia, 1997.

[6] T.O. Mbuya, B.O. Odera, and S.P. Ng'ang'a. Influence of iron on castability and properties of aluminium silicon cast alloys: Literature review. *International Journal of Cast Metals Research*, 16(5):451–465, 2003.

[7] L. Bäckerüd, G. Chai, and J. Tammninen. *Solidification Characteristics of Aluminium Alloys*, volume 2. AFS/Skandaluminium, USA, 1990.

[8] L.A. Narayanan, F.H. Samuel, and J.E. Gruzleski. Crystallization behaviour of Iron-containing intermetallic compunds in 319 aluminium alloys. *Metallurgical and Materials Transactions*, 25A:1761–1773, 1994.

[9] S. Belmares-Perales, M. Castro-Romàn, M. Herrera-Trejo, and L.E. Ramìrez-Vidaurri. Effect of cooling rate and Fe/Mn ratio on volume fractions of α-AlFeSi and β-AlFeSi phases on Al-7.3Si-3.5Cu alloy. *Metals and Materials International*, 14(3):307–314, 2008.

[10] A. Verma, S. Kumar, P.S. Grant, and K.A.Q. O'Reilly. Effect of cooling rate on the Fe intermetallic formation in an AA6063 Al alloy. *Journal of Alloys and Compounds*, 555:274–282, 2012.

[11] W. Khalifa, F.H. Samuel, and J.E. Gruzleski. Iron intermetallic phases in the Al corner of the Al-Fe-Si system. *Metallurgical and Materials Transactions*, 34A:807–825, 2003.

[12] K. Liu, X. Cao, and X.-G. Chen. Effect of cooling rate on iron-rich intermetallic phases in 206 cast alloys. *Light Metals 2013*, pages 311–316, 2013.

[13] S. Shankar, Y.W. Riddle, and M. Makhlouf Makhlouf. Nucleation mechanism of the eutectic phases in aluminium-silicon hypoeutectic alloys. *Acta Materialia*, 52:4447–4460, 2004.

[14] Y.H. Cho, H.-C. Lee, K.H. Oh, and A.K. Dahle. Effect of Strontium and Phosphorus on eutectic Al-Si nucleation and formation of $\beta - Al_5FeSi$ in hypoeutectic Al-Si foundry alloys. *Metallurgical and materials transactions*, 39A:2435–2448, 2008.

[15] G. Sha, K. O'Reilly, B. Cantor, J. Worth, and R. Hamerton. Growth related metastable phase selection in a 6xxx series wrought Al alloy. *Materials Science and Engineering*, A304-306:612–616, 2001.

[16] I. Obinata and N. Komatsu. Phases in alloys of aluminum with iron and silicon. *Journal of the Japan Institute of Metals*, 19(2):197–201, 1955.

[17] H.P. Takeda and K. Mutuzaki. The Equilibrium Diagram of the Iron-Aluminium-Silicon System. *Tetsu-to-Hagane*, 26:335–361, 1940.

[18] G. Phragmèn. The phases occurring in alloys of aluminum with copper, magnesium, manganese, iron, and silicon. *Journal of the Institute of Metals*, 77:489–552, 1950.

[19] H.W.L. Phillips and P.C. Varley. The constitution of alloys of Aluminium with Manganese, Silicon and Iron. *The Journal of the Institute of Metals*, 69(947):317–350, 1943.

[20] W. Khalifa, A.M. Samuel, F.H. Samuel, H.W. Doty, and S. Valtierra. Metallographic observations of β-AlFeSi phase and its role in porosity formation in Al-7%Si alloys. *International Journal of Cast Metals Reserach*, 19(3):156–166, 2006.

[21] Kral, M.V. A crystallographic identification of intermetallic phases in Al-Si alloys. *Materials Letters*, 59:2271–2276, 2005.

[22] L. Lu and A.K. Dahle. Iron-rich intermetallic phases and their role in casting defect formation in hypoeutectic Al-Si alloys. *Metallurgical and Materials Transactions*, 36A:819–835, 2005.

[23] G. Davignon, A. Serneels, B. Verlinden, and L. Delaby. An isothermal section at 550°C in the Al-Rich Corner of the Al-Fe-Mn-Si System. *Metallurgical and Metals Transactions*, 27A:3357–3361, 1996.

[24] Kral, M.V. and McIntyre, H.R. and Smillie, M.J. Identification of intermetallic phases in a eutectic Al-Si casting alloy using electron backscatter diffraction pattern analysis. *Scripta Materialia*, 51:215–219, 2004.

[25] D. Munson. A clarification of the phases occuring in aluminium-rich Aluminium-Iron-Silicon alloys, with particular reference to the ternary phase α-AlFeSi. *The Journal of the Institute of Metals*, 95:217–219, 1967.

[26] D.J. Skinner, R.L. Bye, D. Raybould, and A.M. Brown. Dispersion strengthened Al-Fe-V-Si alloys. *Scripta Metallurgica*, 20:867–872, 1986.

[27] M.A. Rodriguez and D.J. Skinner. Compositional analysis of the cubic silicide intermetallics in dispersion strengthened Al-Fe-V-Si alloys. *Journal of Materials Scince Letters*, 9:1292–1293, 1990.

[28] J.Q. Wang, C.F. Qian, B.J. Zhang, M.K. Tseng, and S.W. Xiong. Valence electron structure analysis of the cubic silicide intermetallics in rapidly solidified Al-Fe-V-Si alloy. *Scripta Materialia*, 34(10):1509–1515, 1996.

[29] K.L. Sahoo, S.K. Das, and B.S. Murty. Frmation of novel microstructures in conventinally cast Al-Fe-V-Si alloys. *Materials Science and Engineering*, A355:193–200, 2003.

[30] G. Jha, F. Cannova, and B. Sadler. Increasing coke impurities - Is this really a problem for metal quality? *Light metals 2012*, pages 1303–1306, 2012.

[31] G. Jha, S. Ningileri, X. Li, and R. Bowers. The challenge of effectively utilizing trace elements/impurities in a varying raw materials market. *Light Metals 2013*, pages 929–934, 2013.

[32] M.A. Rhamdhani, J.F. Grandfield, A. Khaliq, and G. Brooks. Management of impurities in cast house with particular reference to Ni and V. *Light Metals 2013*, pages 33–38, 2013.

[33] J.F. Grandfield, L. Sweet, C. Davidson, J. Mitchell, A. Beer, S. Zhu, X. Chen, and M. Easton. An initial assessment of the effects of increased Ni and V content in A356 and AA6063 alloys. *Light Metals 2013*, pages 39–44, 2013.

[34] Materials Science International Team MSIT and Gautam Ghosh. *Aluminium Iron Silicon*. Springer-Verlag Berlin Heidelberg, 2008.

[35] Materials Science International Team MSIT and Gautam Ghosh. *Aluminium Iron Silicon*. Springer-Verlag Berlin Heidelberg, 2008.

[36] Zi-Kui Liu and Y.A. Chang. Thermodynamic Assessment of the Al-Fe-Si System . *Metallurical and Materials Transactions A*, 30A:1081–1095, 1999.

[37] J.Y. Hwang, H.W. Doty, and M.J. Kaufman. Crystallographic studies on the iron-containing intermetallic phases in the 319-type aluminium casting alloy. *Philosophical Magazine*, 88(4):607–619, 2008.

[38] L.F. Mondolfo. *Aluminium Alloys: Structure and Properties*. Butterworths, 1976.

[39] W. Kurz and D.J. Fisher. *Fundamentals of Solidification*. Trans Tech Publications LTD, 4th edition, 1998.

[40] W. Khalifa, F.H. Samuel, J.E. Gruzleski, H.W. Doty, and S. Valtierra. Nucleation of Fe-intermetallic phases in the Al-Si-Fe alloys. *Metallurgical and Materials Transactions*, 36A:1017–1032, 2005.

[41] EDAX TSL Orientation Imaging Microscopy, OIMDC 5.32Alpha, 2008.

[42] K. Robinson and P.J. Black. An x-ray examination of an α-(Al-Fe-Si) ternary compound. *Philosphical Magazine*, 44:1392–1397, 1953.

[43] R.E. Coelho, S.J.G. de Lima, and F. Ambrozio. Extrusion of aluminium alloys prepared from mechanically alloyed powder. *Materials Science Forum*, 416–418:176–183, 2003.

[44] A.H. Maitland and D. Rodriguez. Vanadium in Aluminium. In *Proceedings of the 8th International Ligth Metals Congress*, pages 423–425, 1987.

[45] J.G. Zheng, R. Vincent, and J.W. Steeds. Crystal structure of an orthorhombic phase in β-(Al-Fe-Si) precipitates determined by convergent-beam electron diffraction. *Philosophical Magazine*, A80(2):493–500, 2000.

[46] C. Rømming, V. Hansen, and J. Gjønnes. Crystal structure of $\beta - Al_{4.5}FeSi$. *Acta Crystallographica*, B50:307–312, 1994.

[47] V. Hansen, B. Hauback, M. Sundberg, C. Rømming, and J. Gjønes. β-Al4.5FeSi: A Combined Synchrotron Powder Diffraction, Electron Diffraction, High- Resolution Electron Microscopy and Single-Crystal X-ray Diffraction Study of a Faulted Structure. *Acta Crystallographica*, B54:351–357, 1998.

[48] P. Villars and L.D. Calvert. *Pearson's Handbook of Crystallographic Data for Intermetallic Phases*. American Society of Metals, 1985.

[49] R.N. Corby and P.J. Black. The Structure of α-(AlFeSi) by Anomalous-Dispersion Methods . *Acta Crystallographica*, B33:3468–3475, 1977.

[50] J. Hjelen. *Scanning elektron-mikroskopi*. Metallurgisk Institutt, NTH, 1989.

[51] Bruker Nano GmbH, Berlin, Germany. *Introduction to EDS analysis - Reference Manual*, April 2011.

[52] Bruker Quantax Espirit 1.9.4.

[53] EDAX-TSL. *OIM DC 5.2*, 1997-2007.

[54] D.P. Field. Recent advances in the application of orientation imaging. *Ultramicroscopy*, 67(2):1–9, 1997.

[55] L. Sweet, S.M. Zhu, S.X. Gao, J.A. Taylor, and M.A. Easton. The effect of iron content on the iron-containing intermetallic phases in a cast 6060 aluminium alloy. *Metallurgical and Materials Transactions*, 42A:1737–1749, 2011.

[56] A.K. Gupta, P.H. Marois, and D.J. Lloyd. Review of the techniques for the extraction of second-phase particles from aluminium alloys. *Materials Characterization*, 37:61–80, 1996.

[57] NORDIF 1.4.0, 2008. EBSD model.

[58] Imagic Image Access easyLab 6, 1992-2006.

[59] A.L. Dons. Alstruc, 2003.

[60] A.L. Dons, E.K. Jensen, Y. Langsrud, E. Trømborg, and S. Brusethaug. The Alstruc microstructure solidification model for industrial aluminium alloys. *Metallurgical and Materials Transactions*, 30A:2135–2146, 1999.

[61] John R. Brown. *Foseco Non-Ferrous Foundryman's Handbook*, chapter 2, page 40. Butterworth Heinemann, 11th edition, 2008.

[62] K. Schäfer and B. Predel. *Binary Systems. Part 1: Elements and Binary Systems from Ag-Al to Au-Tl.*, volume 19B1 of *Landolt-Börnstein: Group IV Physical Chemistry*, chapter 2, page 143. Springer Berlin Heidelberg, 2002.

[63] P Franke and Neuschütz. *Binary Systems. Part 3: Binary Systems from Cs-K to Mg-Zr.*, volume 19B3 of *Landolt-Börnstein: Group IV Physical Chemistry*, chapter 2, page 190. Springer Berlin Heidelberg, 2005.

[64] Walter Borchardt-Ott. *Crystallography: An Introduction*, chapter 7. Springer-Verlag Berlin Heidelberg, 3rd edition, 2011.

[65] Walter Borchardt-Ott. *Crystallography: An Introduction*, chapter 6, 10. Springer-Verlag Berlin Heidelberg, 3rd edition, 2011.

Appendix A

Binary phase diagrams

The binary phase diagrams for Al-Si, Al-Fe and Fe-Si are shown in Figures A.1, A.2 and A.3, respectively. Based on these diagrams there are 9 binary intermetallic phases that can form, theoretically, in addition to the Al-Si eutectic and the metal phases Al and Fe.

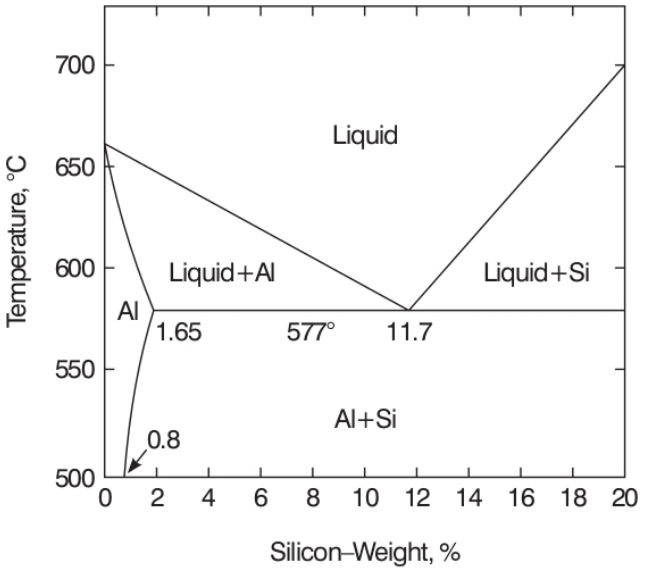

.

Figure A.1: Binary phase diagram for the Al-Si system up to 20wt% Si [61]

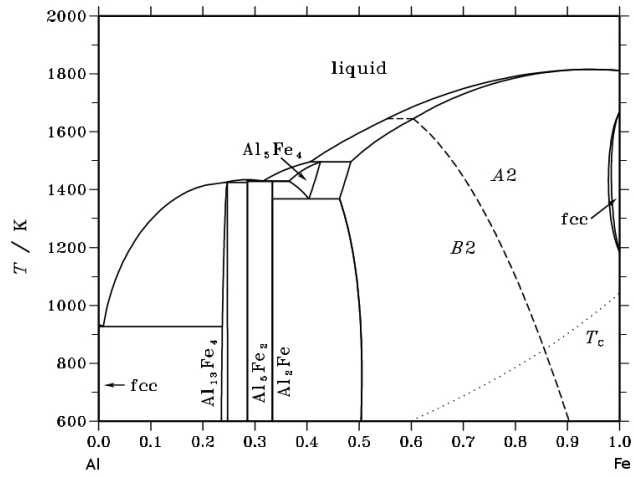

Figure A.2: Binary phase diagram for the Al-Fe system [62]

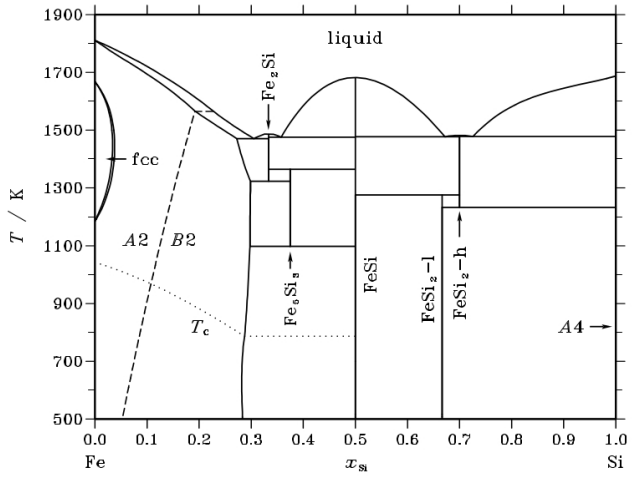

Figure A.3: Binary phase diagram for the Fe-Si system [63]

Appendix B

Crystallography 101 continued

Lattice positions

Within each structure four different groups of atomic positions (lattice points) are defined as listed below. Examples of each is shown for the orthorhombic system is shown in Figure B.1. Depending on this, a total of 14 so-called *Bravais lattices* are possible, as some of the structures are unable to attain some of the lattice point groups.

- **P:** Primitive, lattice points only on the corners of the unit cell.
- **I:** Body centred, primitive with one lattice point at the centre of the cell as well.
- **F:** Face centred, primitive with additional lattice points on each side of the cell.
- **A, B or C:** Base centred, primitive with additional lattice points at two opposing faces.

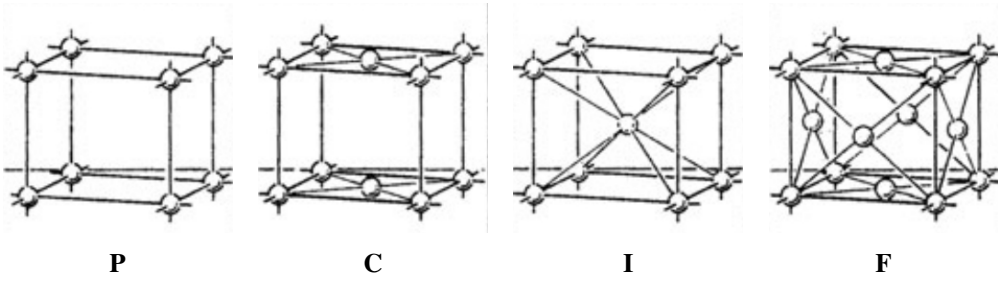

Figure B.1: Example of the four groups of possible lattice points, as listed above, in the orthorhombic structure [64].

Space Groups and Symmetry

In order to describe the crystal structure in more detail, the *space groups* are introduced. The first, capitalized, letter in the space group gives the lattice point group as explained above (cf. Figure B.1). The following numbers and/or letters indicates the symmetry of the structure. A brief overview with explanation is found in Table B.1.

Table B.1: Explanation of symbols and nomenclature found in common space group notation [65].

Symbol	Meaning	Explanation
Number	Rotation Axis	The number represents how many times the structure is equal upon 360° rotation around a relevant axis
m	Mirror Plane	The structure is mirrored around a relevant plane
overlined number (e.g. $\bar{3}$)	Inversion centre	The effect of rotation relative the number followed by an inversion
Subscript on number (N_n)	Screw axis	The main number (N) indicates rotation, the subscript (n) the following translation along the rotation axis (in terms of n/N of the axis length)
Slash (\)	Normal to	Indicates that what stands before the slash is normal to what comes after the slash
a, b or c	Glide plane(s)	Along a-, b- or c-axis relatively
n	Glide plane(s)	Diagonal translation in a plane (halfway along two axes)
d	Glide plane(s)	*Diamond glide*, 1/4 along two axes in a plane
e	Glide plane(s)	Glide plane with possible glide along two axes

Appendix C

HP-Al analysis from supplier

07.10.2004

GDMS-Analysis

Sample Identification: **T1640**

Grade: **Al5N**

Ag	< 5	ppb	Mg	1,41	ppm
As	11	ppb	Mn	47	ppb
B	58	ppb	Mo	< 5	ppb
Ba	< 5	ppb	Na	12	ppb
Be	< 5	ppb	Ni	< 5	ppb
Bi	< 5	ppb	O	< 10,0	ppm
Ca	< 20	ppb	P	526	ppb
Ce	782	ppb	Pb	< 5	ppb
Cl	< 100	ppb	Pd	< 100	ppb
Co	< 5	ppb	Pt	< 100	ppb
Cr	11	ppb	S	< 100	ppb
Cs	< 10	ppb	Sb	< 5	ppb
Cu	2,60	ppm	Si	669	ppb
F	< 100	ppb	Sn	< 50	ppb
Fe	504	ppb	Ti	65	ppb
Ga	< 5	ppb	Th	64	ppb
Ge	< 40	ppb	U	12	ppb
In	< 5	ppb	V	43	ppb
K	< 100	ppb	W	< 25	ppb
La	526	ppb	Zn	< 50	ppb
Li	< 5	ppb	Zr	8	ppb
Cd	< 50	ppb	Nd	148	ppb

Appendix D

SG-Si analysis from supplier

WACKER POLYSILICON

PRODUCT SPECIFICATION

Specification: PCL-LE1 Version: A
Date of Issue: 08.09.2005

Product	HYPER PURE SILICON, POLY, SOLAR APPLICATION Chips, Size 1 (0 – 15 mm), light etched
Supplier	Wacker-Chemie GmbH Polysilicon / Site Burghausen
Manufacturer	Wacker-Chemie GmbH Polysilicon / Site Burghausen

This specification is issued and handled by Wacker-Chemie GmbH Polysilicon Logistics / Site Burghausen; it is valid upon authorized signature by customer and supplier.

agreed upon:

SCANWAFER: _____
Name / Position / Date

Wacker-Chemie GmbH: _____
Name / Position / Date

Wacker-Chemie GmbH: _____
Name / Position / Date

Distribution:

	Scanwafer	Wacker-Chemie GmbH Polysilicon Logistics
Copies	1	1

List of Revisions:

New issue/Change	Description	Date	Revision
New issue		12.05.2005	A

Scanwafer PCL-LE1 Vers A.doc

WACKER POLYSILICON

PRODUCT SPECIFICATION

1. Material of Specification and Application

1.1 This SPECIFICATION describes requirements for solar grade silicon material, which is purchased by CUSTOMER from WACKER.

1.2 In case that either CUSTOMER or WACKER wishes to change all or part of SPECIFICATION, such party will give notice to the other party at least 90 days prior to the date upon which it wishes such change to take effect unless otherwise mutually agreed.

1.3 This SPECIFICATION sets acceptance and rejection criteria for all incoming solar grade silicon material, and supersedes all the previous.

2. Production Method

The delivered silicon chips are produced by Siemens method using trichlorosilane (TCS, SiHCl3) as feed stock gas.

3. Values and Analytical methods

Parameter	Values and Units	Analytical methods	Notes
Bulk purity and Resistivity	Donors (P, As, Sb) Max. 300 ppta Acceptors (B, Al) Max. 100 ppta	Dopants are determined on a floatzoned sample by Photo-luminescence Spectroscopy (FTPL) or by Infrared Absorption Analysis (FTIR).	CZ POLY will be delivered as collective consignment with corresponding collectve lot numbers.
	Carbon Max. 250 ppba	Carbon is determined by Infrared Absorption Analysis (FTIR) on annealed polycrystalline samples.	
	Bulk Metals Total of bulk metals (Fe, Cu, Ni, Cr, Zn, Na) Max. 2 ppbw	Bulk impurities are determined quarterly by applying Neutron Activation Analysis (NAA) to randomly selected pieces of polycrystalline silicon.	
Surface Metals	Fe max. 10 ppbw Cu max. 1 ppbw Ni max. 1 ppbw Cr max. 1 ppbw Zn max. 2 ppbw Na max. 6 ppbw	Surface impurity levels are determined by Inductively Coupled Plasma (ICP), Mass Spectroscopy (MS).	
Resistivity	Bulk + Surface Resistivity Purity N-Type: 100 Ohm*cm Purity P-Type: 1000 Ohm*cm		

Size	Length	Weight	Notes
Size 1	0 – 15 mm	Min. 90 %	No part of rods within 20 mm from electrode is included.

WACKER POLYSILICON

PRODUCT SPECIFICATION

Parameter	Notes
Surface condition	light etched
Surface morphology, Discolourations and Stains	Not specified
Foreign substances	Not allowed
Weight	5 kg ± 50 g per bag
Packing	Double bagging with PE. Each bag individually sealed.
Packing case	6 bags/carton, 8 carton/pallet

4. Labels/Report on Inspection

4.1 Labels on 5 kg bags

The label on the 5 kg bag will give the information about
(1) Manufacturer
(2) Collective lot number
(3) Weight
(4) Guaranteed values for donor and acceptor concentration
(5) Chip size
(6) Poly grade: LE Solar
(7) Article name
(8) Packaging date

4.2 Labels on Cartons

The label on the carton will give the same information as the label on the 5 kg bag except the quantity, here 30 kg.

4.3 Labels on Pallets

The label on the pallet will give the information about
(1) Manufacturer
(2) Collective lot number
(3) Weight of pallet
(4) Specification number

4.4 Delivery Note

To accompany each shipment with the information about
(1) Order number
(2) Quantity / weight of pallets
(3) Collective lot numbers
(4) Specification number
(5) Chip size

4.5 Certificate of Compliance

To accompany each shipment with the information about
(1) Order number
(2) Product name
(3) Guaranteed spec. values for purity and chip size
(4) Package form
(5) Weight of shipment
(6) Signature of authorized person

Scanwafer PCL-LE1 Vers A.doc

5. Procedure of Claim Handling

5.1 Generally claims refer to pallets.
5.2 Upon receiving a notice of quality problem or a claim notice from CUSTOMER, WACKER investigates causes of such problem or claim and issues a corrective action report within 14 days after receiving a sample of the claimed pallet.
5.3 All the costs incurred relating to any rejection set out in this article are born by WACKER.

Appendix E

Alloy preparation calculations

Master alloy calculations

	Al	Si	Fe	V
wt% Si wanted		7.00%		
HP-Al		0.0000669%	0.0000506%	
Master alloy Vanadium			0.30%	10.00%
Masteralloy Fe			5.00%	0.00%

	wt%(V)	wt%(Fe)	m(Al) [g]	m(Si) [g]	m(M-Fe) [g]	m(M-V) [g]	m(tot) [g]
Alloy 7	0.00%	0.30%	475.88	38.288	32.814	0.000	546.983
Alloy 8	0.06%	0.30%	477.13	38.640	32.916	3.312	551.998
Alloy 9	0.20%	0.30%	489.50	40.254	33.809	11.501	575.064
Alloy 10	0.20%	0.30%	487.38	40.080	33.662	11.451	572.574

Control of calculations

	wt%(Si)	wt%(V)	wt%(Fe)
Alloy 7	7.000%	0.000%	0.300%
Alloy 8	7.000%	0.060%	285.826%
Alloy 9	7.000%	0.200%	952.054%
Alloy 10	7.000%	0.200%	952.054%

Master alloy actual weights

	m(Al) [g]	m(Si) [g]	m(M-Fe) [g]	m(M-V) [g]	m(tot) [g]
Alloy 7	475.88	38.298	32.821	0	546.999
Alloy 8	477.13	38.656	32.924	3.319	552.029
Alloy 9	489.5	40.263	33.815	11.51	575.088
Alloy 10	487.38	40.087	33.667	11.46	572.594

Theoretical composition

	wt%(Si)	wt%(V)	wt%(Fe)
Alloy 7	7.00%	0.00%	0.30%
Alloy 8	7.00%	0.06%	0.30%
Alloy 9	7.00%	0.20%	0.30%
Alloy 10	7.00%	0.20%	0.30%

Appendix F

Ion Milling

Ion milling was tested as an EBSD-preparation technique. In order to obtain the best ion milling result 4 different parameters (listed below) were tested. All used an eccentricity of 5mm (maximum). Two examples of milling results obtained can be seen in Figure F.1, indicating that option (a) gave the best surface finish.

Upon testing EBSD it appeared that the ion milling results were good for aluminium and silicon. For the iron rich intermetallics, however, the signal was not strong enough to obtain a good EBSD-pattern.

(a) 78° tilt for 30 minutes and $0.08cm^3/min$ gas flow

(b) 78° tilt for 60 minutes and $0.08cm^3/min$ gas flow

(c) 80° tilt for 30 minutes and $0.08cm^3/min$ gas flow

(d) 80° tilt for 60 minutes and $0.08cm^3/min$ gas flow

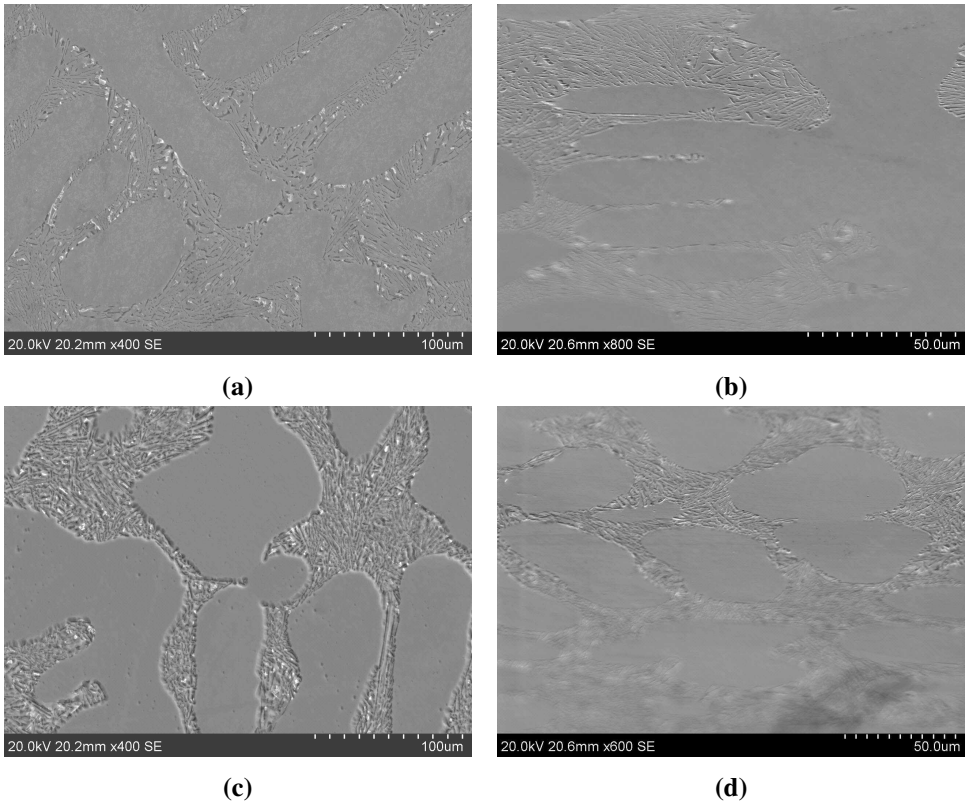

Figure F.1: Images of tilted and untilted examples showing the results of the ion mill preparation technique. (a) and (b) Good milling obtained by 78° tilt for 30 minutes, untilted and tilted respectively. (b) and (c) Bad milling, here represented by 80° tilt for 30 minutes, untilted and tilted respectively.

Appendix G

Chemical analysis from Hydro Aluminium AS

Alloy		Fe	V	Si
	1	0.092	0.00037	6.94
	1	0.092	0.00037	6.92
	1	0.091	0.00038	6.85
	1	0.092	0.00037	6.90
Alloy 1 average		**0.09**	**0.00**	**6.90**
	2	0.261	0.00057	6.91
	2	0.264	0.00056	6.90
	2	0.263	0.00056	6.83
	2	0.263	0.00056	6.88
Alloy 2 average		**0.26**	**0.00**	**6.88**
	5	0.087	0.050	6.79
	5	0.088	0.050	6.87
	5	0.089	0.051	6.88
	5	0.088	0.050	6.85
Alloy 5 average		**0.09**	**0.05**	**6.85**
	6	0.259	0.052	6.85
	6	0.263	0.052	6.83
	6	0.262	0.053	6.84
	6	0.261	0.053	6.84
Alloy 6 average		**0.26**	**0.05**	**6.84**
	3	0.089	0.150	6.83
	3	0.085	0.151	6.66
	3	0.089	0.150	6.89
	3	0.088	0.149	6.76
Alloy 3 average		**0.09**	**0.15**	**6.78**
	4	0.257	0.171	6.83
	4	0.257	0.172	6.78
	4	0.257	0.172	6.84
	4	0.257	0.172	6.82
Alloy 4 average		**0.26**	**0.17**	**6.82**

Appendix H

Particle area fraction of entire image

Table H.1: Total average area fraction of script-and needle-like particles relative to the entire image.

Alloy	Script-like particles [area%]	Needle-like particles [area%]	Total of particles [area%]
High cooling rate (0.9 K/s)			
0V	0.72	0.05	0.77
600ppm V	1.28	0.19	1.25
0.2wt% V	0.60	0.17	0.77
Low cooling rate (0.3K/s)			
0V	0.26	0.97	1.23
600ppm V	0.44	0.71	1.15
0.2wt% V	0.38	0.30	0.68
0.2wt% V + GR	0.04	0.13	0.68

Appendix I

Script identification in 0.2wt% V

Below follows an obtained (SE) micrograph I.1 with indications of where point EDS analysis was done and EDS-results for a intermetallic script-like particles in the 0.2wt% V alloy. The corresponding EDS results are given in Table I.1 and an EDS spectrum is found in Figure I.2. The Fe/Si and Al/Si ratios suggests a phase close to Al_6Fe_2Si. EDS maps of Al (a), Si (b), Fe (c) and V (d) is shown in Figure I.3. The particle is seen to be Fe-rich and a significant amount of V is accumulated.

EBSD indexing was attempted for several script like particles in the alloy, all V-rich. The indeexing was unsuccessful for hexagonal α-$Al_8Fe_2Si)$ in all cases, yielding very poor CIs.

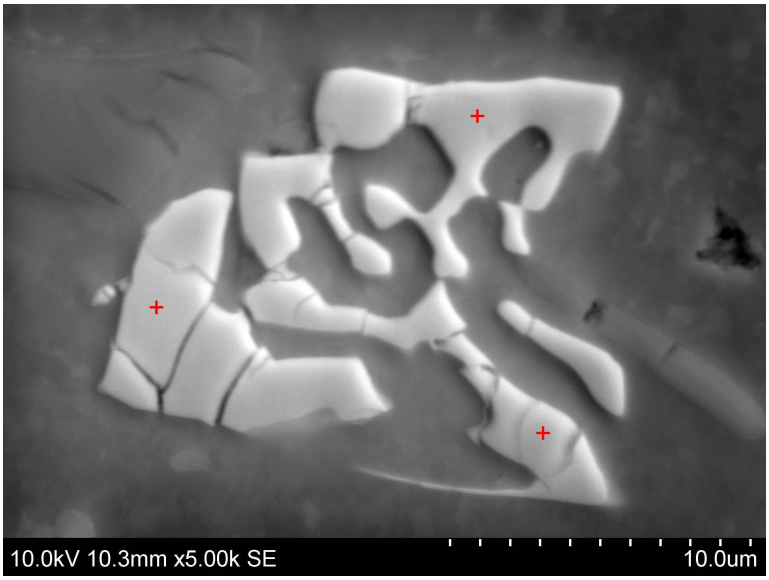

Figure I.1: SE micrograph of a script-like intermetallic particle in the low cooling rate, 0.3wt% Fe and 0.2wt% V alloy. The red crosses indicate points were EDS analysis was conducted. The EDS results are shown in Table I.1. The light grey particles seen around the particle is eutectic Si.

Table I.1: The quantification results for the EDS conducted on the three points shown in Figure I.1. One of the representative spectra obtained and used for quantification is shown in Figure I.2. There is V measured in the particle.

	Al [at%]	Si [at%]	Fe [at%]	V [at%]	Fe/Si	Al/Si
Analysis 1	69.3	10.8	18.9	1.0	1.8	6.4
Analysis 2	65.8	10.9	21.6	1.7	2.0	6.0
Analysis 3	68.4	10.7	19.4	1.5	1.8	6.4
Average	67.8 ±1.8	10.8±0.1	20.0±1.4	1.9±0.1	1.9±0.1	6.1±0.2

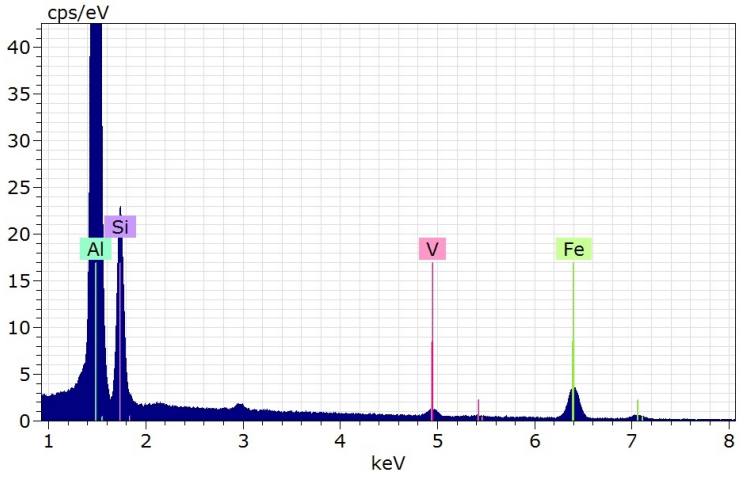

Figure I.2: A representative EDS-spectrum of one of the points on the intermetallic particle shown in Figure 4.17. The spectrum shows a peak for Fe and a peak for V.

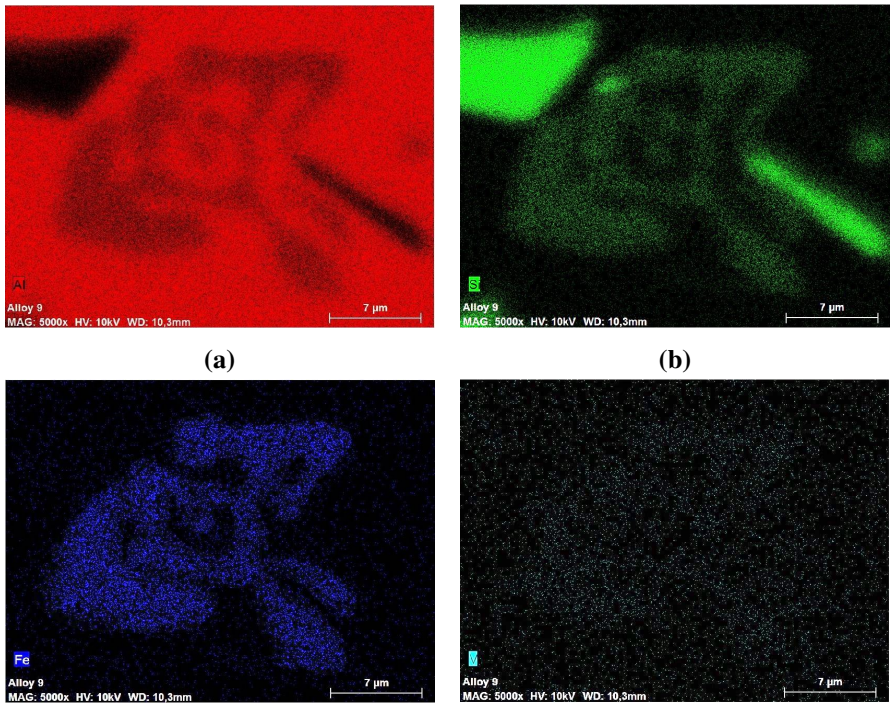

Figure I.3: EDS maps of the particle shown in Figure I.1; (a) Al, (b) Si, (c) Fe and (d) V. The particle contains Al, Si and Fe and shows accumulation of V in the particle. Silicon particles are observed around the particle (b).